Monitoring Beam Backgrounds at Belle II with Scintillator Detectors

by

Helena Pikhartová

McGILL UNIVERSITY

Department of Physics, Faculty of Science

August 2017

A thesis submitted to McGill University in partial fulfillment of the requirements of the degree of Master of Science

McGill University

Abstract

Faculty of Science
Department of Physics

Master of Science

by Helena Pikhartová

This thesis describes the design of a system of fast scintillation detectors arrayed around the Belle II interaction region with the goal of monitoring all major sources of accelerator beam-related background including injection background during the operation of Belle II. Belle II is a high-luminosity b quark factory facility located at the SuperKEKB electron-positron collider at the KEK laboratory in Japan. The main goal of Belle II is the search for evidence of new physics beyond the standard model of particle physics, through measurements of CP violation, rare decays, and searches for forbidden decays. It will improve the sensitivity to new physics by 1 to 2 orders of magnitude compared to previous B factory experiments. Belle II is currently in its commissioning phase, with first physics collisions planned for 2018. Due to higher beam currents and smaller beam sizes, beam-related backgrounds will be larger in Belle II than the ones experienced in Belle, the predecessor experiment of Belle II. Because these backgrounds can result in radiation damage and degraded detector performance due to high occupancy, real-time monitoring of backgrounds rates is essential.

Université McGill

Abrégé

Faculté des Sciences
Département de Physique

Maîtrise en Sciences

par Helena Pikhartová

Cette thèse décrit la conception d'un système de détecteurs à scintillation rapide répartis en réseau autour du point d'interaction du détecteur Belle II. L'objectif du réseau est de surveiller les sources principales de bruit générées par l'accélérateur dont le bruit d'injection qui survient pendant le fonctionnement de Belle II. Le détecteur Belle II est une usine à quarks b opérant à haute luminosité situé au collisionneur électron-positron SuperKEKB du laboratoire KEK au Japon. L'objectif principal du détecteur Belle II est la recherche de preuves de nouveaux phénomènes physiques au-delà du modèle standard de la physique des particules par la mesure de la violation de la symétrie CP, des désintégrations rares et par la recherche de désintégrations interdites. Une amélioration de la sensibilité à de la nouvelle physique de 1 à 2 ordres de grandeur par rapport aux usines à quarks b précédentes est prévue. Belle II est actuellement dans la phase de mise en service, les premières collisions physiques étant prévues pour 2018. Étant donné les plus grands courants et la plus petite taille des faisceaux, le niveau de bruit causé par le fonctionnement du collisionneur sera plus grand avec le détecteur Belle II que ce qui a été observé avec son prédécesseur, le détecteur Belle. Une surveillance du taux de bruit est essentielle puisqu'il peut causer des dommages par radiation ainsi qu'une détérioration de la performance du détecteur due à la haute occupation.

Acknowledgements

I would like to thank my supervisor Dr. Steven Robertson for giving me this opportunity of research, for his expertise and guidance and also help with writing this thesis. I would like to express my gratitude to Dr. Hiroyuki Nakayama, the leader of my project, for the opportunity to work with him and his help with my work. I am very grateful to be part of the Belle II collaboration and the BEAST II working group. During the course of my project, many people were very kind to help me with different aspects of my work. Specifically, I would like to thank Andrea Fodor for her help with the beam background simulation, Waleed Ahmed for introducing me to the Geant4 toolkit, Benoit Lefebvre for help with hardware and C++ problems and Michael Hedges for computing advices and insights into the BEAST II group. Lastly, I would like to thank my family for all their support.

Contribution of author

The project of scintillator detectors for measuring beam background at Belle II was an existing project under the supervision of H. Nakayama (KEK). My contribution was an upscale and upgrade of the project. Specifically I contributed to engineering drawings and design of attachment structure and cable path, QCS drawing update, simulation (with different conditions as simulation was upgraded during the time of research), analysis of the simulation, implementing the scintillator volume in the Geant4 simulation of the Belle II detector, testing of hardware and testing of readout. This work is presented in Chapters 4 and 5.

Contents

List of Figures

List of Tables

Abbreviations

BEAST II	**B**eam **E**xorcism for **A** **ST**able Belle **II** experiment
SM	**S**tandard **M**odel
NP	**N**ew **P**hysics
SAD	**S**trategic **A**ccelerator **D**esign
IP	**I**nteraction **P**oint
HER	**H**igh **E**nergy **R**ing
LER	**L**ow **E**nergy **R**ing
ARES	**A**ccelerator **R**esonantly coupled with **E**nergy **S**torage
SCC	**S**uper **C**onducting **C**avity
RF	**R**esonant **F**requency
PXD	**Pix**el **D**etector
SVD	**S**ilicon **V**ertex **D**etector
CDC	**C**entral **D**rift **C**hamber
ECL	**E**lectromagnetic **Cal**orimeter
PID	**P**article **I**dentification **D**etector
ACC	**A**erogel **C**herenkov **C**ounter
TOF	**T**ime **O**f **F**light
PMT	**P**hoto-**M**ultiplier **T**ube
MPPC	**M**ulti-**P**ixel **P**hoton **C**ounter
ADC	**A**nalog to **D**igital **C**onverter
FPGA	**F**ield-**P**rogrammable **G**ate **A**rray
TDC	**T**ime to **D**igital **C**onverter

Chapter 1

Introduction

Belle II is a particle physics experiment [1]. It is administrated by an international collaboration of over 600 physicists from 23 countries. Located at the KEK (Japanese High Energy Accelerator Research Organization) laboratory in Japan [2], Belle II is an upgrade of its predecessor, the Belle experiment. The Belle II detector is placed at the interaction point of the SuperKEKB accelerator. The interaction point (IP) is the point along the accelerator ring at which the two counter-rotating beams are caused to intersect, resulting in collisions between electrons and positrons. The experiment is currently in the commissioning stage and is planned to start collecting data at the end of 2018.

The Belle experiment was operating between the years 1998 and 2010 [3]. Between these years, it had accumulated a data sample corresponding to an integrated luminosity of 1000 fb^{-1} (containing around 1 billion $B\overline{B}$ pairs). One of its accomplishment was the observation of CP violation in the B meson system (also observed by the BaBar experiment [4] during the same year), a theory that led to the Nobel Prize award for physicists M. Kobayashi and T. Maskawa in 2008 [5].

The Belle II experiment aims to collect an even larger data sample than Belle due to its plan for increased luminosity. The upgrade will also improve performance of the detector to manage higher particle flux rates.

This thesis describes the design and simulation of beam background monitoring detectors. These detectors will be implemented around the final focusing magnets (QCSs) in the vicinity of the interaction point of the Belle II detector. Chapter 2 introduces the theory

of particle physics, the standard model, and the problems of this theory. It presents the concept of a particle passage through matter and the beam backgrounds. Chapter 3 is the overview of the SuperKEKB accelerator and the Belle II detector. It also introduces the commissioning detector (BEAST II). Chapter 4 describes the scintillator sensors that are installed to monitor the beam background at the Belle II detector. It introduces the technology that makes it an optimal sensor type to use, and specifies the positioning and readout. Chapter 5 talks about the simulation of beam backgrounds with regards to the scintillator detectors. Chapter 6 outlines the future work that will be done after completion of this thesis. Chapter 7 concludes this thesis.

Chapter 2

Theory

The Belle II experiment is aiming to find evidence of the presumable physics beyond the standard model in decays of heavy flavor particles, and in particular in the decays of B mesons. Belle II will study collisions of electrons and positrons at the center of mass energy of $\sqrt{s} = 10.58$ GeV (where $\sqrt{s}$ is the combined energy of positrons and electrons in the lab frame at the collision point). Data taking is also anticipated to include collisions at other center of mass energies, as well as studies of tau leptons, charm quarks, QED processes, dark sector searches, quarkonium, and exotic states.

This chapter introduces the standard model of particle physics and its unresolved problems, the passage of particles through matter, and the background signals created in the accelerator.

2.1 Standard model and beyond

The SM of particle physics governs the major forces of our universe that are relevant at the subatomic scale: the electromagnetic, weak, and strong forces. It also describes all known elementary particles. The gravitational force is not included in this model as its effects are negligible at these scales.

The SM of particle physics consists of fermions (leptons and quarks), gauge bosons, and the Higgs boson. SM describes the interactions of elementary fermions via three fundamental forces (electromagnetic, weak, strong), described by gauge fields, and including

a scalar Higgs field. The forces are mediated by the exchange of vector gauge bosons associated with a (spontaneously broken, by the Higgs field) $SU(2)_L \times U(1)_Y$ and $SU(3)_C$ gauge symmetries.

Leptons comprise the electron, muon, and tau particles (with negative electric charge) and also the electron neutrino, the muon neutrino, and the tau neutrino (with zero electric charge). For each of these particles, there is also an anti-particle with opposite quantum numbers. Quarks come in six "flavors" or types: up (u), down (d), charm (c), strange (s), top (t), and bottom (b). They have fractional electric charge ($+2/3$, $-1/3$) and their anti-particles are the anti-quarks with opposite charges. In contrast to leptons, quarks carry color charge and are therefore affected by the strong force. Quarks cannot be observed alone, due to the color confinement property of the strong interaction, and together form hadrons. Hadrons can be divided into mesons (containing two quarks) and baryons (containing three quarks). Gauge bosons are the carriers of the fundamental forces. The electromagnetic force is mediated by the photon. The carriers of the weak force are the $W^{\pm}$ and Z^0 bosons. The strong force is mediated by the gluons.

Although the SM is the currently recognized theory of particle physics, there are reasons to believe that it is incomplete, suggesting the existence of new physics beyond the SM. These come out of questions that the SM cannot answer. The SM describes matter as we know it (elementary particles, atoms, elements, ..). However, this form of matter makes up only 5% of the observable universe. The rest consists of 70% of dark energy, which has only been inferred to exist via effects on cosmological scales, and 25% of dark matter, which has been observed (exclusively via gravitational interactions in astronomical measurements), but could be made of matter not described by the SM [6]. Another example, the hierarchy problem, presents the unnaturally large discrepancy between the characteristics of the weak and gravitational forces. The mass of the weak force carriers (the Z and W bosons) is about 10^{16} times smaller than the Planck mass ($m_p = \sqrt{\frac{\hbar c}{G}} \sim 2.2 \times 10^{-8}$ kg). This giant difference is the source of searches for theoretical explanations [7].

Belle II will search for evidence of physics beyond the Standard Model by making precise measurements of any deviations from the SM and by searching for strongly suppressed decay processes.

2.2 Physics at B factories

Belle II is a B factory laboratory; a lepton collider experiment optimized for producing and analyzing B mesons.

The Belle II experiment is a collider experiment that accelerates and collides electrons and positrons. The energies of the electrons and positrons are chosen in order to create a large number of B mesons. B mesons are particles that are composed of a b anti-quark and one of u, d, c, s quarks. In the case of Belle II, the energy of electrons is initially chosen to be 7 GeV and the energy of positrons 4 GeV, which corresponds to a center of mass energy of the $\Upsilon(4S)$ resonance. The $\Upsilon(4S)$ is a resonance of bottomonium, a meson containing a b and an anti-b quark. Its rest mass is 10.58 GeV [1] and in 95% of cases, it decays into a pair of $B\overline{B}$ mesons [8].

2.3 Interactions of particles with matter

Detection of subatomic particles is possible through particle interactions with matter. These interactions depend on the type of incident particle (heavy/light, charged/neutral, hadron vs lepton/photon). To detect most of them, general purpose detectors, such as Belle II, with a variety of subdetector technologies are built.

2.3.1 Interactions of charged particles

Electrically charged particles are connected to the electromagnetic force (in addition, charged hadrons also interact via the strong force). Charged leptons interact with matter mostly via ionization and excitation. Relativistic charged particles also lose energy from Bremsstrahlung radiation. Other interactions include direct pair production, photonuclear interactions, Cherenkov radiation, or transition radiation [9]. There are a large variety of detectors aimed at detecting charged particles, including ionization chambers, scintillation counters, Cherenkov light detectors and others. These interaction mechanisms are discussed below.

[1] Mass is expressed in units of GeV because $\hbar$ =c= 1

2.3.1.1 Ionization and excitation

Both excitation and ionization consist of inelastic scattering of an incident particle in the electric field of a nucleus. The incident particle loses energy, which is subsequently radiated as a photon or ionized electron. A characteristic equation of excitation (and subsequent de-excitation via radiation) can be expressed as:

$$f^{-+} + atom \rightarrow f^{-+} + atom^{*} \rightarrow f^{-+} + atom + \gamma \tag{2.1}$$

where f^{-+} is any charged fermion. In the case of ionization, the incident particle will completely separate an electron from the atom:

$$f^{-+} + atom \rightarrow f^{-+} + atom^{+} + e^{-}. \tag{2.2}$$

The incident particle will lose some of its energy to the ionization/excitation. The average energy loss dE per unit distance traveled through a medium dx is expressed by the Bethe formula [10]:

$$-\left\langle \frac{dE}{dx} \right\rangle = \frac{4\pi}{m_e c^2} \cdot \frac{nz^2}{\beta^2} \cdot \left(\frac{e^2}{4\pi\varepsilon_0} \right)^2 \cdot \left[\ln\left(\frac{2m_e c^2 \beta^2}{\mathrm{I} \cdot (1-\beta^2)} \right) - \beta^2 \right] \tag{2.3}$$

where

n = Electron number density
z = Charge of incident particle
e, m_e = Charge, mass of electron
ϵ_0 = Permittivity of free space
I = Mean excitation energy
c = Speed of light
β = Velocity of incident particle / Speed of light.

Energy loss is proportional to the material density and independent of the mass of the incident particle [11]. An example of an ionization detector is the proportional chamber, a device that collects and analyzes charge produced by an incident particle ionizing the detector material [12].

2.3.1.2 Bremsstrahlung

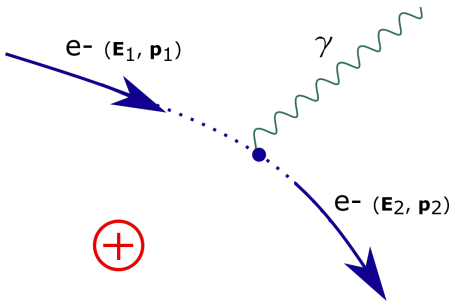

FIGURE 2.1: Bremsstrahlung radiation diagram.

Charged particles with high velocity also lose energy through the Bremsstrahlung process in addition to ionization and excitation. Nuclei of material produce an electric field which can decelerate the traversing particle. The lost kinetic energy will then be emitted in the form of photons (Figure 2.1). The energy loss in this process can be characterized by the equation [13]:

$$\frac{dE}{dx} \approx 4\alpha\ N_A\ \frac{Z^2}{A}\ z^2(\frac{1}{4\pi\epsilon_0}\ \frac{e^2}{mc^2})^2\ E\ ln\frac{183}{Z^{1/3}} \tag{2.4}$$

where

Z, A = Atomic number, atomic weight of the medium
z, m, E = Charge number, mass, energy of the incident particle.

Unlike the energy loss by ionization, the energy loss of Bremsstrahlung is proportional to the characteristics of the incident particle, its energy and mass. Bremsstrahlung is especially important for electrons, due to their small mass.

2.3.2 Interactions of photons

In contrast to charged particles, photons pass freely through matter or they are completely absorbed in a material which will then emit other photon or different particles. That is, they cannot lose only part of their energy in an interaction.

Figure 2.2 shows the photon cross section for interactions with light and heavy elements (carbon and lead) [14]. The following sections present three most prominent photon interaction types: the photoelectric effect, Compton scattering and pair production.

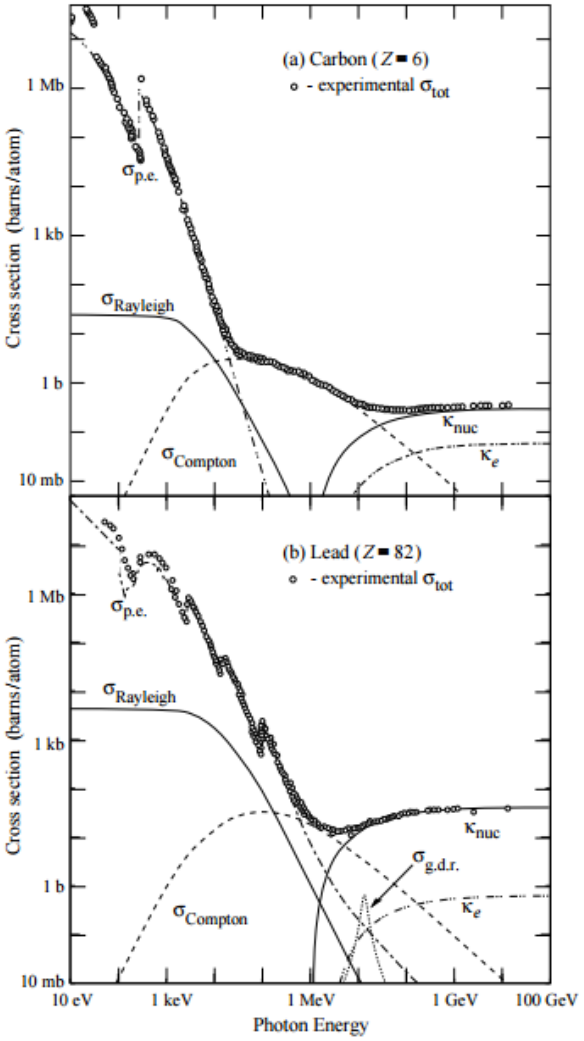

FIGURE 2.2: Total photon cross section in carbon and lead, as a function of energy, showing the contributions of different processes:
$\sigma_{p.e.}$ atomic photo-effect (electron ejection, photon absorption)
$\sigma_{Rayleigh}$ coherent scattering (atom neither ionized nor excited)
$\sigma_{Compton}$ incoherent scattering (Compton scattering off an electron)
κ_{nuc} pair production, nuclear field
κ_e pair production, electron field
$\sigma_{g.d.r}$ = photonuclear absorption

2.3.2.1 Photoelectric effect

Photons of certain wavelength can be absorbed in a material which can then free an electron (Figure 2.3) [15]. The photoelectric effect cross section is very large for low energy photons.

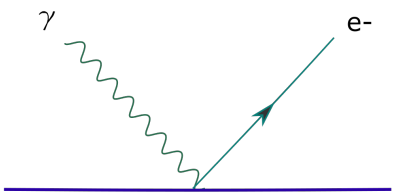

FIGURE 2.3: Photoelectric effect diagram.

The energy of the escaped electron depends on the wavelength of the photon (λ) and the metal work function (W):

$$E = \frac{hv}{\lambda} - W \tag{2.5}$$

This type of process is used, for example, in photomultiplier (PMT) technology. PMTs detect photons which produce photoelectrons which are then studied to infer the properties of the initial photons.

2.3.2.2 Compton scattering

For photons of intermediate energies (E $\sim$ 1 MeV), the main process of interactions is Compton scattering. It is an inelastic scattering of a photon off of a free electron or other charged particle. The charged particle gains energy while the photon's wavelength increases [16]. A characteristic equation is:

$$\gamma + e^- \rightarrow \gamma' + e^- \tag{2.6}$$

A simple diagram is shown in Figure 2.4:

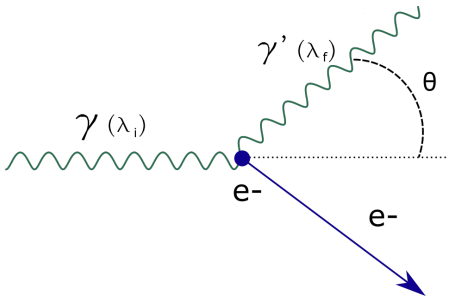

FIGURE 2.4: Compton Scattering diagram.

The change of wavelength of the scattered photon can be expressed as:

$$\lambda_f - \lambda_i = \frac{h}{m_e c}(1 - \cos\theta) \tag{2.7}$$

where λ_f and λ_i are the final and initial wavelengths and θ is the scattering angle.

2.3.2.3 Pair production

For higher energies the most dominant interaction of photons is pair production. In this process, a photon is near a nucleus, its energy can be converted into an electron-positron pair (Figure 2.5) [17]. It is a transformation of radiant energy into matter.

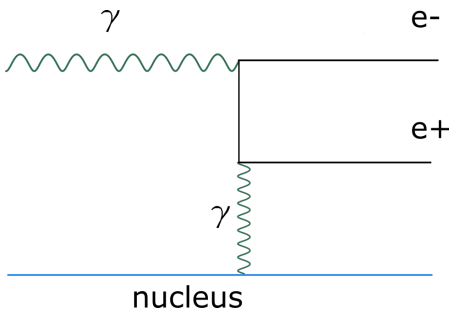

FIGURE 2.5: Pair production diagram.

Ignoring the recoil energy of the nucleus, the electron positron pair obtains kinetic energy which equals the energy of the photon minus the rest masses of electron and positron:

$$K(e^-) + K(e^+) = hf - 2(m_e c^2) \tag{2.8}$$

where:

f = Photon frequency
m_e = Rest mass of electron.

2.3.3 Electromagnetic showers

An electromagnetic shower happens if a high-energy electron, positron or photon (mostly through Compton scattering and pair production) interact with a material. High energy electrons and positrons emit photons through Bremsstrahlung. These photons then

Compton scatter or pair produce into new electrons/positrons. This process continues until the photon energy is below the threshold for pair production and the electron/-positron energy is sufficiently low that ionization dominates over Bremsstrahlung. The result is a cascade of ionizing particles and photons that rapidly lose all of their energy in the material. This energy deposition can be collected in the form of charge, scintillation light etc. and exploited in calorimeter detectors to determine the energy of the incident particle.

Muons have greater mass than electrons and don't produce as much Bremsstrahlung radiation, as can be inferred from equation 2.4.

2.4 Accelerator and Beam Backgrounds

The SuperKEKB accelerates electrons and positrons so that Belle II can study their collisions. An overview of SuperKEKB is presented in Section 3.1.

In the ideal SuperKEKB collider, electrons and positrons are accelerated and collided to create B meson pairs and other interesting particle interaction phenomena, with no additional particles produced in the event to complicate the detector reconstruction of the interaction. In reality, there are other particle interactions produced in the accelerator, which still reach the detector volume. These affect both the operation of the collider as well as the final data collected by the detector. It is therefore important to understand and monitor these "beam background" sources.

Beam backgrounds are the unwanted interactions created by the electrons and positrons in the beam prior to or in addition to the physics interactions of interest. There are many types of background created at different points of the accelerator. Beam background is created as a result of injection of bunches into storage rings, intra-bunch effects, interactions with residual gas in the beam pipe, and bending and focusing the beam. Electron-positron collisions at the interaction point which produce particles only outside the detector acceptance region which hit the beamline components and shower into the detector are also considered beam background.

Although background is generated at various places along the collider beam pipe, the beam backgrounds considered by Belle II are those that propagate towards, or are created

in the vicinity of, the Belle II detector and consequently have the potential to produce occupancy or radiation damage in the detector. The next sections present the most dominant beam background sources produced by a lepton collider.

2.4.1 Touschek effect

One of the most dominant sources of beam background at the Belle II detector is the Touschek effect [18]. The collision of two particles within one bunch at a large angle could transfer part of their transverse momentum into longitudinal momentum. The scattered particles then have lower or higher energy than the bunch and therefore the accelerator magnet lattice and RF acceleration shift their trajectory on a different orbit radius. They are then ejected from the beam bunch and collide with the beam pipe (Figure 2.6).

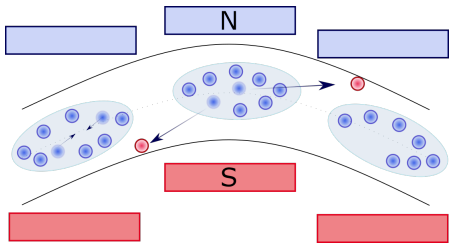

FIGURE 2.6: Touschek effect diagram.

The probability of Touschek scattering is given by the Møller differential cross section:

$$\frac{d\sigma}{d\Omega} = \frac{r_0^2}{4\gamma^2}((1+\frac{1}{\beta^2})^2(\frac{4}{\sin^2\Phi} - \frac{3}{\sin^2\Phi}) + \frac{4}{\sin^2\Phi} + 1), \tag{2.9}$$

where

r_0 = Radius of electron
β = Velocity/speed of light of incident particle
Φ = Scattering angle.

Integrating the Møller cross section at leading order over the solid angles, the Touschek lifetime (time until the beam loses all of its current due to the Touschek effect) can be calculated as:

$$\frac{1}{\tau} = \left\langle \frac{r_0^2 cN}{8\pi\gamma^2\sigma_x\sigma_y\sigma_z\delta_{acc}^3} D(\epsilon) \right\rangle \tag{2.10}$$

where N is the number of particles in a bunch, γ is the Lorentz factor, σ_x, σ_y and σ_z are bunch width, height and length, δ_{acc} is the momentum acceptance. D(ϵ) is defined as:

$$D(\epsilon) = \sqrt{\epsilon}\,[-\frac{3}{2}\,e^{-\epsilon} + \frac{\epsilon}{2}\int_{\epsilon}^{\infty}\frac{\ln u}{u}e^{-u}du + \frac{1}{2}(3\epsilon - \epsilon\ln\epsilon + 2)\int_{\epsilon}^{\infty}\frac{e^{-u}}{u}du]$$
$$\epsilon_m = (\frac{\delta_{acc}}{\gamma\sigma_{x'}})^2$$

Averaging over the whole accelerator ring and assuming that δ_{acc} is constant, the Touschek lifetime can be scaled as:

$$\tau \propto \frac{\sqrt{\epsilon_y}\sigma_z}{I}\delta_{acc}^3 \tag{2.11}$$

In summary, the rate of Touschek background is proportional to the beam size, the number of bunches and the bunch current [19].

2.4.2 Beam-gas scattering

Beam-gas scattering occurs when beam particles interact with residual gas atoms or molecules in the beam pipe (Figure 2.7). The rate of beam-gas background is proportional to the pressure inside the beam pipe (P), the beam current (I) and the charge of the residual particles (z):

$$\frac{dN}{dt} \propto IPz^2 \tag{2.12}$$

Two types of beam-gas scattering are the Coulomb and Bremsstrahlung radiation.

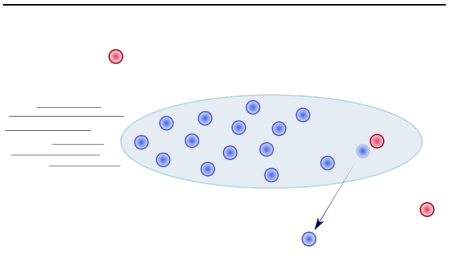

FIGURE 2.7: Beam gas scattering diagram.

Coulomb scattering with a gas nucleus doesn't emit particles, but the direction of the electron/positron is changed. The differential cross section of this process can be expressed as [20]:

$$\frac{d\sigma_{coulomb}}{d\Omega} = \frac{Z^2\alpha^2}{4\beta^2|\vec{p}|^2 sin^4\frac{\theta}{2}}, \tag{2.13}$$

where

Z = Charge of gas nucleus
$\beta, \vec{p}$ = Velocity/speed of light, momentum of incident particle
α = Fine structure constant
θ = Scattering angle.

In the case of Bremsstrahlung, the particle emits a photon and decreases its energy. The differential cross section of this process is:

$$\frac{d\sigma_{brem}}{d\epsilon} = \frac{r_0^2\alpha Z[Z+\xi(Z)]}{\epsilon}([1+(1-\epsilon)^2][\Phi_1(\delta)-F(Z)] - \frac{2}{3}(1-\epsilon)[\Phi_2(\delta)-F(Z)]) \tag{2.14}$$

where E is the energy of incident particle, ϵ is the fraction of E transfered to a photon, θ is the scattering angle, Z is the atomic number and δ, Φ_1 and Φ_2 are defined as:

$$\begin{aligned}
\delta &= \frac{136m_e}{Z^{1/3}E}\frac{\epsilon}{1-\epsilon} \\
\Phi_1 &= 20.867 - 3.242\delta + 0.625\delta^2 \qquad \text{for} \delta \leq 1 \\
\Phi_2 &= 20.209 - 1.930\delta + 0.086\delta^2 \qquad \text{for} \delta \leq 1 \\
\Phi_1 &= \Phi_2 = 21.12 - 4.184\ln(\delta + 0.952) \qquad \text{for} \delta > 1 \\
\xi(Z) &= \frac{\ln(1440/Z^{2/3})}{\ln(183/Z^{1/3}) - f_c(Z)} \\
f_c(Z) &= Z\alpha(\frac{1}{1+Z\alpha} + 0.20206 - 0.0369Z\alpha + 0.0083(Z\alpha)^2 - 0.002(Z\alpha)^3) \\
F(Z) &= \begin{cases} 4/3\ln ZE & : E < 0.05\text{GeV} \\ 4/3\ln Z + 4f_c(Z)E & : E \geq 0.05\text{GeV}. \end{cases}
\end{aligned}$$

In addition to the "base" pressure of the rings, the circulation of the beams can cause gas molecules to desorb from the inner surface of the beampipe, causing a "dynamic" pressure that scales with the beam currents. Running the beams for a long time eventually desorbs all the available gas (a procedure called "vacuum scrubbing"), causing the vacuum quality to improve with time.

2.4.3 Synchrotron radiation

Synchrotron radiation occurs when electrons and positrons are deflected in a magnetic field. These then emit photons (Figure 2.8). Synchrotron radiation is one of the limiting factors for the final energy of the accelerated particles in an electron-positron collider. It is proportional to the velocity of the accelerated particles and inversely proportional to the radius of curvature.

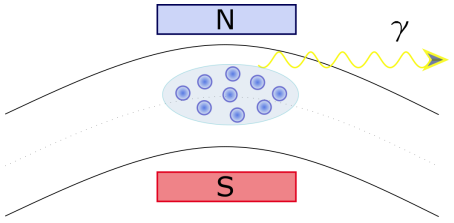

FIGURE 2.8: Synchrotron radiation diagram.

Synchrotron radiation photons from magnets in the vicinity of the IP can illuminate sensitive detector components. The large energy contained in synchrotron radiation needs to be carefully disposed of by precise design of machine elements and dedicated masking.

2.4.4 Bhabha background

Electron-positron scattering is also known as Bhabha scattering. Bhabha scattering is considered to be beam background if the scattered particles at the interaction point do not enter the detector volume, but instead interact with the beam pipe and produce other particles (via electromagnetic showering), which enter the detector instead.

Electron-positron scattering can also create photons in the initial or final state. One of many possible Feynman diagrams is shown in Figure 2.9. The electron or positron loses some of its energy and produces background by hitting the beam pipe or even scattering

inside the detector area. The cross section of radiative Bhabha increases as the energy of the emitted photon decreases.

The cross section of Bhabha scattering becomes largest when the angle of scattering approaches 0°. This results in a very high rate of low-energy and low-angle particles. The scattered particles hit machine elements downstream of the IP, which then shower back into the detector.

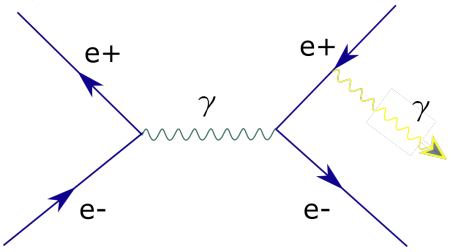

FIGURE 2.9: Radiative Bhabha scattering diagram.

The Bhabha scattering process is proportional to the luminosity. It is widely used in electron-positron collider experiments for accurate luminosity measurement.

2.4.5 Injection background

At SuperKEKB, the beam is injected in the storage rings continuously ("top-up injection"). After two beam bunches are collided, they are refilled with new particles. As the particles enter the storage rings, they are placed inside the preexisting bunch. If this process isn't performed precisely, the injected particles' emittance is larger that the one of the already circulating bunch, hence it takes a while for the topped-up bunch to damp down to the nominal beam emittance, which it does by radiating and scattering inside the beampipe. This type of background has distinctive time structure (compared to other more uniform background sources), corresponding to the circulation time of the bunch going around the storage ring. The newly-injected bunch decays exponentially due to synchrotron radiation and by collisions with movable collimators.

There is currently no simulation of the injection background behavior. It is therefore important to monitor the background in real time.

Chapter 3

SuperKEKB and the Belle II experiment

3.1 SuperKEKB

The SuperKEKB accelerator is the upgrade of the KEKB collider with the goal of obtaining a data sample with an integrated luminosity of 50 ab^{-1}, a factor of 50 higher than KEKB. The luminosity is the measure of the expected rate of particle interactions. This luminosity will be achieved by running at the instantaneous luminosity of $8 \times 10^{35} cm^{-2} s^{-1}$, the world highest instantaneous luminosity ever achieved (compared to other high energy accelerators in Figure 3.1). The expected rate for the $\Upsilon(4S) \to B\overline{B}$ is 960 Hz and the integrated luminosity sample will contain around 2.4×10^7 $B\overline{B}$ pairs (cross section of this process is 1.2 nb).

3.1.1 Accelerator Overview

The main parts of the SuperKEKB collider are the LINAC accelerator, positron damping ring, and the storage rings.

The SuperKEKB accelerator accelerates electron and positrons. Electrons are created by an RF electron gun (a high intensity laser is applied to an alloy which produces electrons via the photoelectric effect). These are then accelerated by the linear accelerator LINAC. The LINAC accelerates electrons to 7 GeV and positrons to 4 GeV. In the next step,

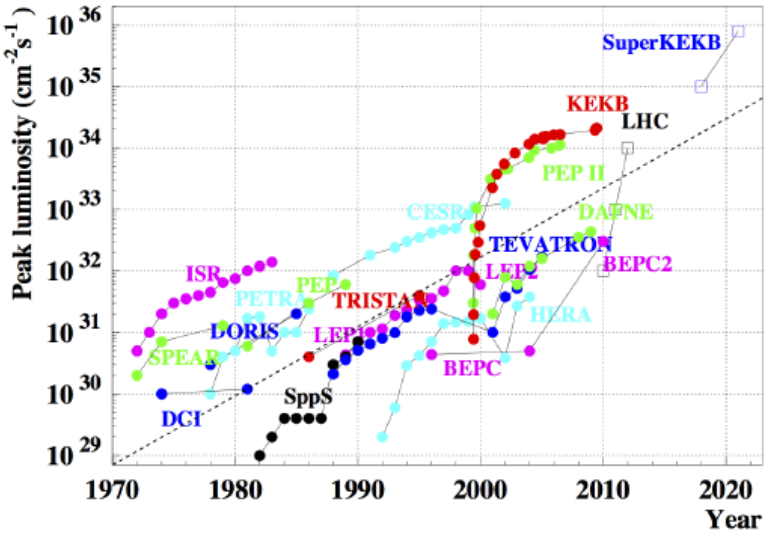

FIGURE 3.1: Comparison of luminosity achieved and planned by different particle physics experiment.

electrons are injected into the high energy storage ring (HER). Positrons are created from electrons hitting a tungsten target located at the beginning of the LINAC. The formed positrons then continue to the damping ring. This extra stage guarantees low emittance of the positron bunches (the final emittance is around 2.5% of the initial emittance [21]). Positrons then follow the same path as electrons through the LINAC and are injected into the low energy storage ring (LER). SuperKEKB uses continuous injection, where bunches of electrons/positrons enter the storage rings with help of electromagnets with fast-varying magnetic fields. The rate of injection is 25 Hz [22]. The circumference of the storage rings is 3 km. The number of bunches per ring is 2503 with revolution frequency of 99.4 kHZ and bunch spacing of 4 ns. The energies of the beams at design luminosity will be 7.01 and 4.0 GeV for HER and LER respectively.

A diagram showing the SuperKEKB accelerator is shown in Figure 3.2.

The bending and focusing of the beams is done using around 1000 quadrupole magnets, 220 bending magnets, 200 sextupole magnets and 1100 correction magnets which are placed around the main storage rings.

For acceleration, SuperKEKB uses the ARES (Accelerator Resonantly coupled with Energy Storage) cavities and SCC (Super Conducting Cavity) cavities. The RF frequency of these devices is 508.887 MHz [18].

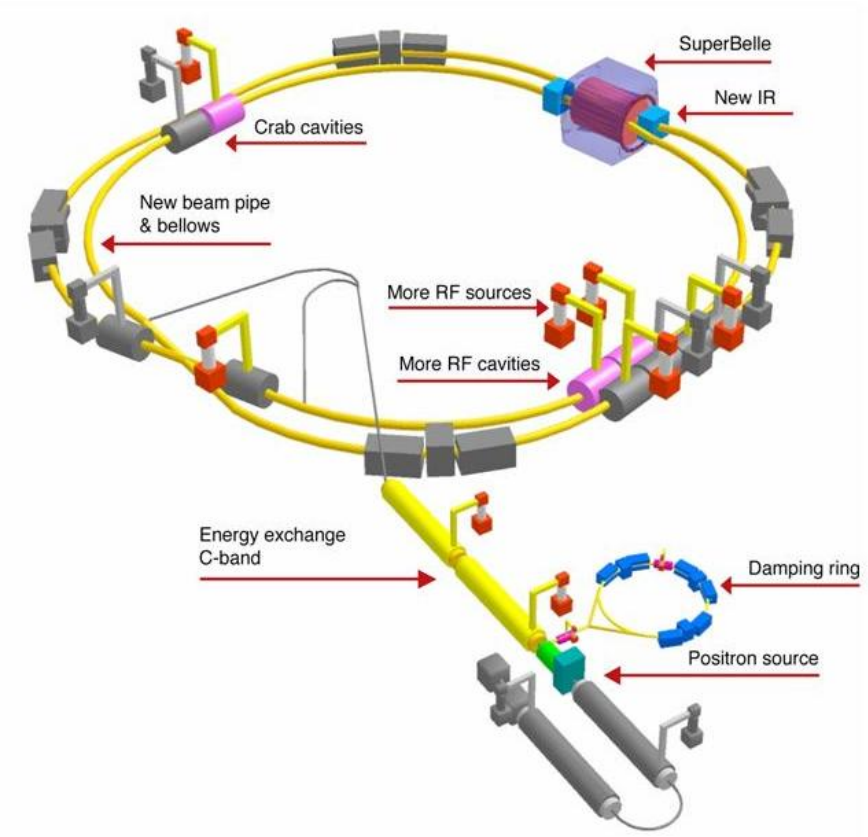

FIGURE 3.2: Diagram of the SuperKEKB accelerator showing positions of important parts as well as the Belle II detector (here written as SuperBelle).

3.1.2 Accelerator Upgrade

SuperKEKB is reusing many parts of the KEKB accelerator, such as the storage rings. In order to achieve much larger luminosity, many parts had to be upgraded and their operation improved. The proposed improvements compared to the KEKB design and achieved values are presented in Table 3.1.

The luminosity can be expressed as:

$$L = \frac{\gamma_{\pm}}{2er_e}(1 + \frac{\sigma_y^*}{\sigma_x^*})(\frac{I_{\pm}\xi_{y\pm}}{\beta_y^*})(\frac{R_L}{R_{\xi_{y\pm}}}) \tag{3.1}$$

where

γ = Lorentz factor

β = Vertical beta function at the IP

$\sigma_{y/x}$ = Vertical/horizontal beam size at IP

ξ_y = Beam-beam parameter

$+/-$ = Positron/electron

I = Beam current

R_{L/ξ_y} = Reduction factors for the luminosity / vertical beam-beam parameter.

Beam Parameters	KEKB achieved		SuperKEKB design	
	LER	HER	LER	HER
Energy [GeV]	3.5	8.0	4.0	7.01
Beam current [A]	1.64	1.19	3.6	2.62
ξ_y	0.129	0.090	0.087	0.081
β_y^* [mm]	5.9	5.9	0.27	0.30
σ_y^* [nm]	940	940	48	60
σ_x^* [μm]	147	170	10	10
Beam lifetime [min]	200	133	10	10
Luminosity [10^{34} cm^{-2} s^{-1}]	2.108		80	

TABLE 3.1: Design parameters for the SuperKEKB operation compared to the KEKB achieved parameters.

In order to achieve the world record luminosity, the SuperKEKB accelerator is using the nano beam scheme [23]. The vertical beam size at the interaction point is designed to be 48 and 60 nm (LER and HER). Also, the beam currents will be increased. Many new superconducting cavities and magnets are installed and another large improvement is the interaction point setup with new quadrupole superconducting magnets (QCS) working on final focusing of the beams.

3.2 Belle II Detector

The Belle II detector is a multi-purpose detector with cylindrical geometry located at the interaction point of the SuperKEKB accelerator. It is also an upgrade of the Belle detector.

The coordinate system of the Belle II detector, which is observed within this thesis is shown in Figure 3.3. The x axis is horizontal and towards the outside of the SuperKEKB storage rings. The y axis is vertical and pointing upwards. The z axis is defined by the

Belle II solenoid axis (positive z in approximately in the direction of the electron beam). ϕ is the azimuthal angle with $\phi = 0$ at $(x, y, z) = (1, 0, 0)$ and θ is the zenith angle with $\theta = 0$ at $(x, y, z) = (0, 0, 1)$.

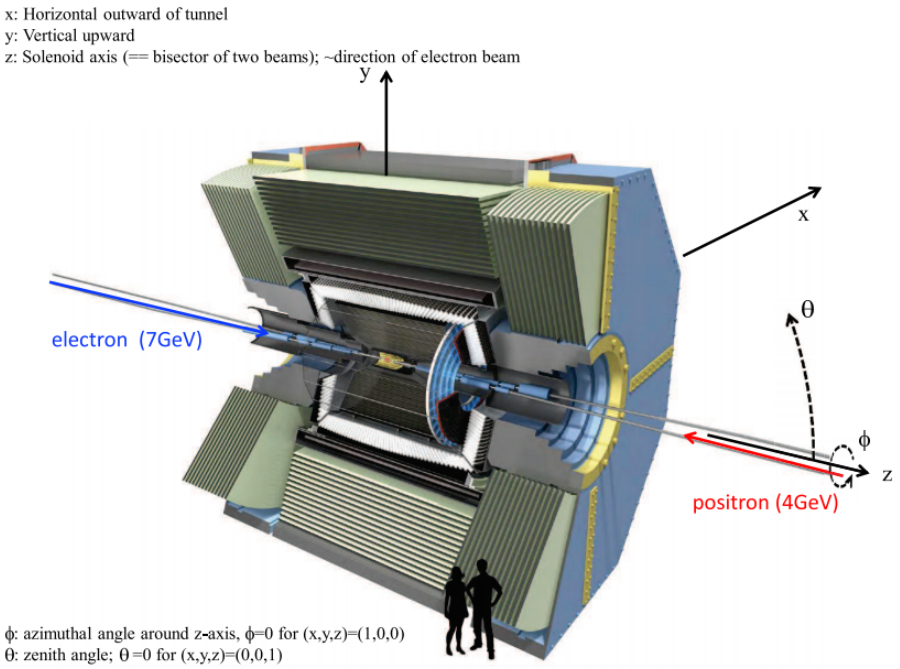

FIGURE 3.3: The coordinate system of the Belle II detector.

The particles produced by the interactions of electrons with positrons at the interaction point propagate outwards passing through successive layers of detectors designed to measure their properties. The inner layers provide precise spatial tracking of charged particles, which can be used for reconstruction of primary and secondary vertex positions. A 1.5 T solenoid magnet causes charged particles to bend, enabling the determination of their momenta. Denser outer detectors stop and measure the energy of electrons and photons, while muons are identified by their ability to penetrate into the outermost layers.

In order to achieve its physics goals, the Belle II detector is being upgraded from the Belle detector. The upgrade will serve for handling increased particle flux and background rates, and improve physics performance.

3.2.1 Detector overview

The Belle II detector contains these subdetectors: pixel detector (PXD), silicon vertex detector (SVD), central drift chamber (CDC), particle identification detector (PID), electromagnetic calorimeter (ECL), and a detector for K_L^0 and muons (KLM). A top view of the detector is shown in Figure 3.4.

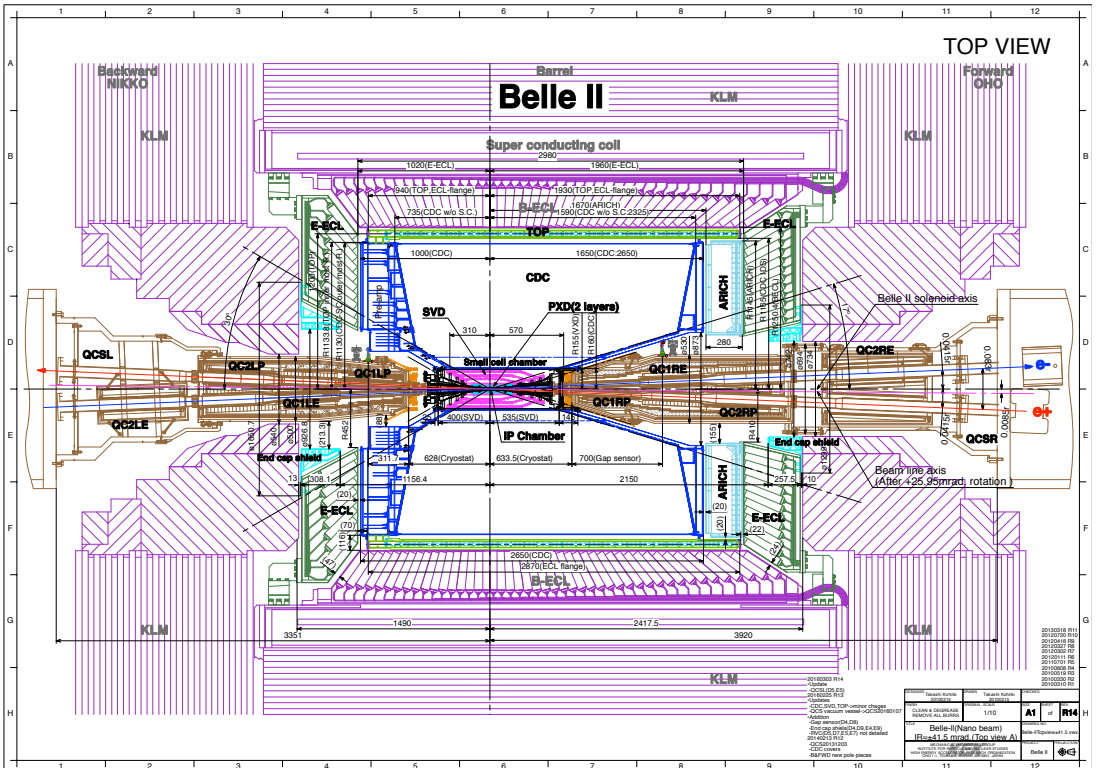

FIGURE 3.4: The horizontal cross section of the Belle II detector at the level of the interaction point.

The innermost layer is the vertex detector (VXD) consisting of the PXD and the SVD. The PXD is composed of two cylindrical layers of silicon pixels 14 and 22 mm from the interaction point. The SVD has 4 layers spaced from 38 to 140 mm from the interaction point. It is made of silicon strips. Both the PXD and SVD have an excellent space resolution ($\sigma_x = 1.3$ μm $\sigma_y = 1.2$ μm for PXD) and will serve to identify secondary vertices and charged particle tracks.

The CDC surrounds the vertex detectors. It is made of over 14000 sense wires in a helium based gas which cover the radius up to 1130 mm from the interaction placed in 56 layers. The CDC serves for reconstructing charged particle tracks and particle

identification from the energy loss in the gas volume. The spatial resolution of CDC is about 100 μm.

The PID combines the information obtained by three subdetectors: the Time Of Propagation (TOP) in the barrel, the Aerogel Ring-Imaging Cherenkov detector (ARICH) in the end-caps, and the CDC. It combines the number of photoelectrons (information about Cherenkov photons radiated in ARICH), the Cherenkov angle and the ionization energy loss provided by the respective detectors. The TOP system is made of quartz-based Cherenkov detectors coupled to micro-channel plate PMTs. The ARICH is located in the forward endcap parts with inner and outer radii of 410 mm and 1140 mm respectively. The Cherenkov light produced in these counters is then collected by an array of position sensitive photon detectors.

The ECL consists of 8736 CsI(Tl) crystals in the barrel and endcap regions. Scintillation light produced by muons (via ionization) and by electrons and photons (through electromagnetic showers) is detected by PIN photodiodes. Electrons and photons are stopped in its volume and the ECL can identify their trajectory and energy. Charged pions will tend to hadronically shower in the ECL, but on average, only about 1/3 of the pion energy is collected in the ECL and the rest propagates to the muon detector layer. Muons, neutrinos and most K_L^0s continue through the whole ECL volume (while losing only a small amount of energy). For these particles, the ECL collects information about their trajectory (for neutrinos, there is no trajectory information, although their 4-vector can be inferred from the total missing energy in the event, which is calculated in part using ECL information).

The KLM is placed outside the superconducting solenoid and is the last layer of the Belle II detector. It consists of layers of thick iron plates to stop particles traveling outward and resistive plate counters that detect particles. Muons are identified based on a pattern of hits in successive layers of the KLM that penetrate the full depth of the detector in a continuous track. K_L^0s produce a more distributed pattern characteristic of a hadronic shower.

3.2.2 Detector Upgrade

The Belle II detector is reusing some systems build for the Belle detector. These include the solenoid magnet, calorimeter crystals, iron yoke, and the muon system. All other parts are newly constructed.

The Belle II experiment will improve its vertex resolution due to the spatial resolution of the two first pixel layers of the detector. The efficiency for reconstructing secondary decays will improve because of the larger volume of silicon strip detector. There are new particle identification detectors in the barrel and endcap regions. And lastly, the new electronics of the ECL provides less electronic noise and improved feature reconstruction.

3.3 Commissioning

The Belle II experiment is currently in its commissioning stage, which ensures a smooth start of the experiment. The commissioning is split in three phases. The time line is shown in Figure 3.5.

To measure the beam backgrounds originating from the SuperKEKB accelerator, the BEAST II (Beam Exorcism for A STable Belle II experiment) commissioning detector was build and placed around the interaction point. It is a set of specialized detectors using different technologies to study beam backgrounds.

The goal of the BEAST II detector is to characterize the beam background, predict radiation doses for Belle II subdetectors and create a baseline for background simulation.

3.3.1 Phase 1

The first phase of the Belle II experiment commissioning was carried out between February and June 2016. At this time the SuperKEKB accelerator was turned on for the first time, and positrons and electrons made their first turns around the storage rings.

In Phase 1, the electron and positron beam were turned on separately. They passed through the interaction point without colliding. The BEAST II detectors were installed around the beam pipes in order to study the backgrounds (Figure 3.6). The different subdetectors of the BEAST II are summarized in table 3.2.

FIGURE 3.5: Schedule of commissioning of the Belle II experiment.

System	Detectors Installed	Type of Measurement
PIN Diodes	64	Neutral vs charged radiation dose
Diamond Sensors	4	Ionizing radiation dose
Micro-TPC's	4	Fast neutron flux
He-3 tubes	4	Thermal neutron flux
LYSO/CsI crystals	18	EM energy, Injection background
BGO crystals	8	Luminosity
CLAWS	8	Injection background

TABLE 3.2: BEAST II Phase 1 subdetector list with primary purpose of each detector.

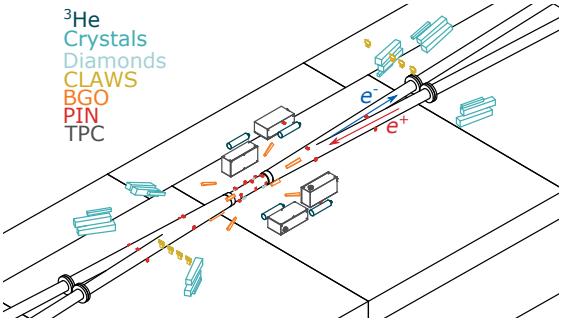

FIGURE 3.6: Positioning of the BEAST II detector around the beam pipes.

The results of BEAST II Phase 1 include measurement of background levels near the IP (excluding luminosity dependent background as Phase 1 was non-collision running). The detector provided important information about the correlation of accelerator parameters

to the beam background conditions. Studies focused on vacuum conditions, injection, beam current and others and measured the influence of these parameters on beam background. Since the conclusion of Phase 1, the beam loss simulations were greatly improved [24].

Leading to Phase 2, many factors will change. The beam currents will increase. New parts of the SuperKEKB accelerator will be installed, such as the final focusing magnets. This will affect the rate and distribution of background. The Belle II detector will be present, which leaves less space for beam background monitors. And finally, electron and positron bunches will be colliding, hence luminosity background sources will be present.

3.3.2 Phase 2

Due to the presence of the Belle II detector, the position of the BEAST II detector will be confined into limited space during Phase 2.

The subdetectors of Phase 2 are presented in Table 3.3. The Belle II PXD and SVD systems are prototypes used before the full installation in Phase 3. The detectors which were used in Phase 1 and will be staying in Phase 2 will continue with their designed purpose (as shown in Table 3.2). New detectors will be added: FANGS is used for injection backgrounds, timing studies and also for VXD commissioning; PLUME is a general purpose radiation sensor; scintillator sensors (most relevant to this thesis) will be measuring general background rates as well as injection background and FPGAs will be monitoring the effects of beam background on electronics and therefore are placed nearest to the beam pipe.

Most detectors (Belle II PXD, Belle II SVD, diamond, CLAWS and PLUME sensors) will be located in the region that will be occupied by the VXD in Phase 3. The PIN diodes and scintillator sensors will be installed around the QCSs (final focusing magnets) and the FPGAs will be directly on the beam pipe. Other detectors such as the Micro TPC's and He-3 tubes will be in the "dock space" located next to the Belle II detector, and one beam monitor (LYSO) will be placed inside the ECL endcap shields.

This thesis focuses on a system of scintillator beam background monitors. The information about its layout, technology, readout system and simulation results is presented in the following chapters.

System	Detectors Installed	Location
Belle II PXD	2 ladders	VXD
Belle II SVD	4 ladders	VXD
Diamond sensors	8	VXD
FANGS	3 arms, 15	VXD
CLAWS	2 ladders	VXD
PLUME	2 ladders	VXD
PIN diodes	40	QCS
Scintillator sensors	40	QCS
Micro-TPC's	8	Dock
He-3 tubes	4	Dock
FPGA	2 boards	SuperKEKB beam pipe
LYSO crystals	8	ECL endcap shield

TABLE 3.3: BEAST II Phase 2 subdetector list with respective positions.

3.3.3 Phase 3

In Phase 3, the Belle II detector will be fully present and running, therefore the BEAST II detector will be reduced to fewer background monitors. The scintillator detectors will remain in place for the whole time of Belle II operation.

3.4 Beam backgrounds at Belle II

With the implementation of the nano-beam scheme, background will increase significantly in the vicinity of the Belle II detector compared to the original Belle experiment, as higher beam currents increase beam-gas background, smaller beam sizes result in increased Touschek background and higher luminosity increases radiative Bhabha background.

The beam background can negatively affect the detector. Some parts of detector are sensitive to radiation damage, such as the silicon pixel detector, calorimeter crystals, CDC and TOF. Beam background also affects the detector occupancy (number of hits before the detector is saturated, different for each subdetector).

The dominant sources of background at the Belle II detector are expected to come from the Touschek effect, Coulomb scattering and Bhabha radiation.

There are some structural solutions that can partially lower beam background. The strategy to deal with Touschek effect background is to install movable horizontal and

vertical collimators. These will absorb the scattered particles before they reach the vicinity of the detector. Since the particles have less or more energy than the nominal beam energy, it is sufficient to use horizontal collimation as dipole bending magnets will spatially separate these in the horizontal plane. Simulation studies indicate that the rate of Bremsstrahlung scattering is lowered by horizontal collimators which results in negligible rate in the detector compared to the Touschek effect. Coulomb scattering background is also lowered by horizontal collimators, however the rate of scattering is still expected to be 100 times larger than during operation of KEKB [25]. Radiative Bhabha flux is reduced by tungsten shielding around the beam pipes, however this shielding is only present very near the interaction point ($< |65|$cm). Synchrotron radiation is taken care of by the design of the beam pipe geometry near the interaction point so that the background does not penetrate into the detector volume.

The impact of the beam background on the Belle II detector can be simulated within the Belle II software framework. The beam loss simulations are generated using the complete accelerator design.[26]. Results of simulations of the beam background in the scintillator sensors are presented in Chapter 5.

Chapter 4

Scintillator Sensors

Scintillator detectors located around the final focusing magnets (QCS) will be installed along with the BEAST II commissioning detector during the Phase 2 commissioning period, and will remain in place throughout the remainder of the Belle II experimental program. The scintillators' relative positions within the Belle II detector are shown in Figure 4.1.

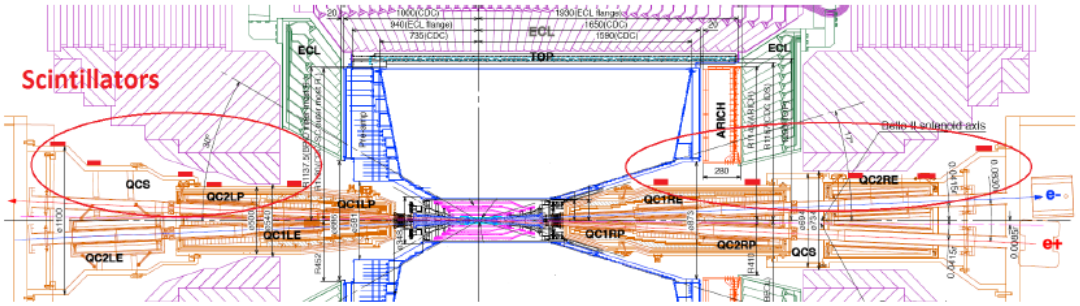

FIGURE 4.1: Simplified diagram showing location of the scintillation sensors within the Belle II detector.

The purpose of these sensors is to measure beam background in the vicinity of the IP. The strategy for completing this project within the dedicated time was to determine locations, design attachments and cable routing, program and test readout, and simulate the performance. This effort is presented in the remainder of this chapter and in Chapter 5.

4.1 Technology

The scintillator detectors must provide information about real time beam background conditions. The more specific requirements include excellent time resolution, radiation hardness, and hardware satisfying space constraints within the detector.

Scintillation is a type of luminescence producing a distinctive spectrum of light after absorption of radiation in a specific material (shown in Figure 4.2). The radiation comes from recombination and de-excitation of atoms in the medium after they have been ionized or excited by a charged particle traversing the medium. Scintillators are usually made of an inorganic (e.g. CsI) or organic (e.g. anthracene) material which has an electronic structure suitable for luminescence.

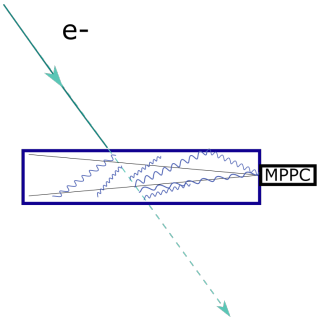

FIGURE 4.2: The concept of scintillation created in a scintillator.

This project uses plastic scintillators, a type of organic material in which the fluorescent emitter (fluor) is present in a polymer base. The specific polymer used is polyvinyltoluene (PVT). An image of the scintillator counters wrapped in light protective foil is shown in Figure 4.3. The size of each scintillator is 10 cm x 4 cm x 1 cm.

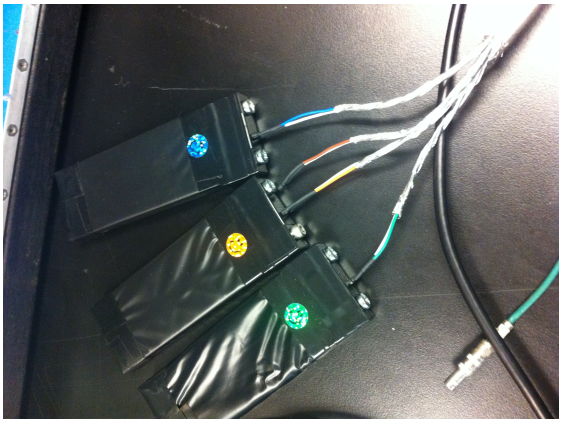

FIGURE 4.3: Scintillator sensors.

The scintillation light produced in the plastic scintillators is collected by a silicon photodetector, a multi-pixel photon counter (MPPC). A silicon photodetector is a type of photoelectric photodetector. The collected photons interact with electrons from the valence band of the semiconductor and shift into the conduction band, resulting in a measurable electric current. This specific type uses multiple avalanche photodiode (APD) pixels in Geiger mode. Geiger mode refers to the operation of the photodiode with a reverse-bias voltage much above the breakdown voltage. The operating voltage in our case is 67V [27]. A technical drawing and a real image are presented in Figure 4.4 [28].

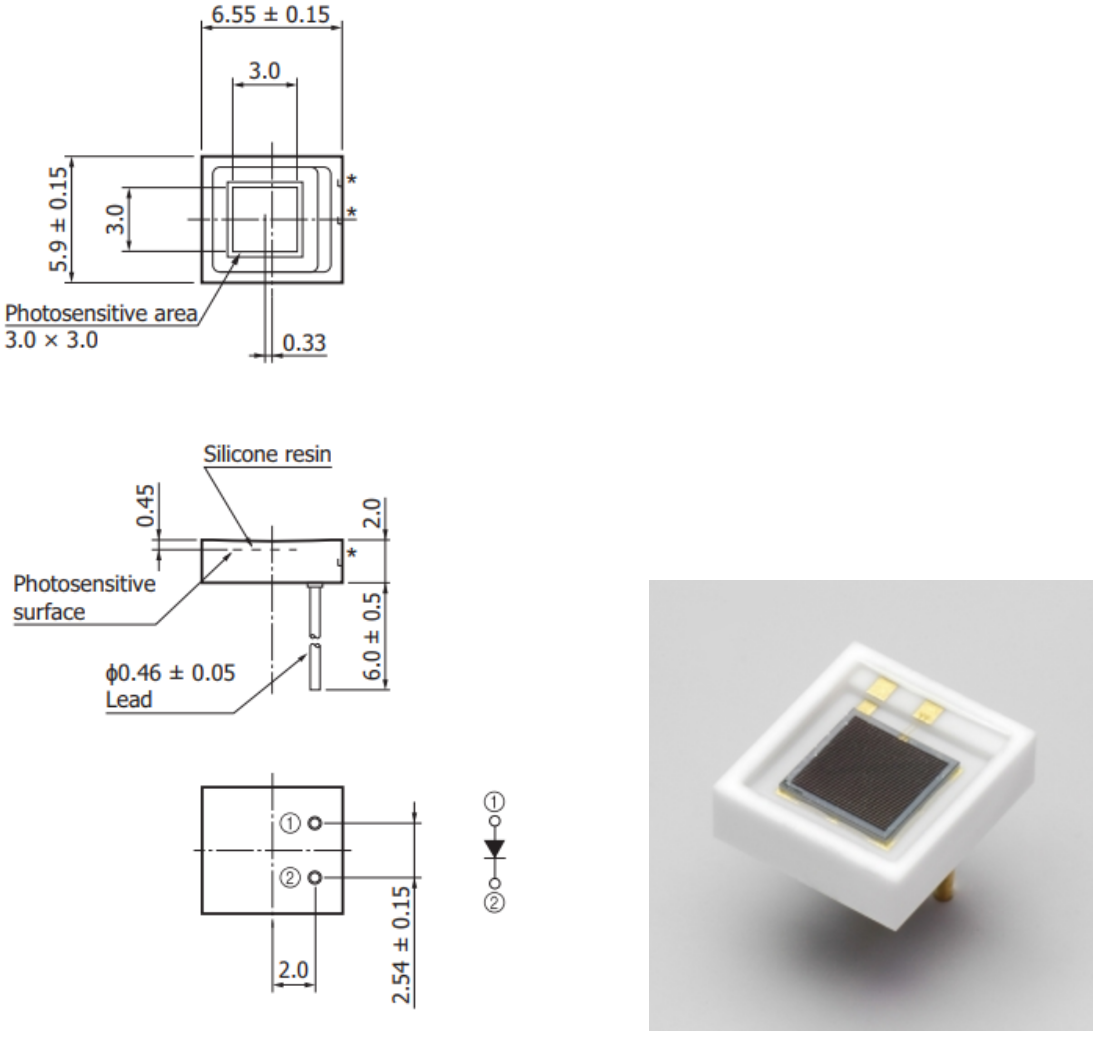

FIGURE 4.4: Diagram of the MPPC technical drawing with measurements and the orientation of the diode on the left with the real image of the MPPC on the right.

There are many advantages to this choice of technology. Scintillators are sensitive to all relevant beam background sources since they all produce ionizing charged particles. The MPPC readout is fast, with nanosecond time resolution, and has excellent photon

counting capability. In addition, the detector is immune to magnetic fields and mechanical shocks. It is also affordable considering there are 40 detectors used. The important characteristics of the MPPC detector is summarized in Table 4.1. A plot describing the photon efficiency as a function of wavelength is shown in Figure 4.5 [28].

Parameters	Effective photosensitive area	Number of pixels	Spectral response range λ	Photon detection efficiency
MPPC S13360-3025CS	3×3 mm	14400	$270 - 900$ nm	25%

TABLE 4.1: Characteristics of the MPPC used in the beam background monitoring setup.

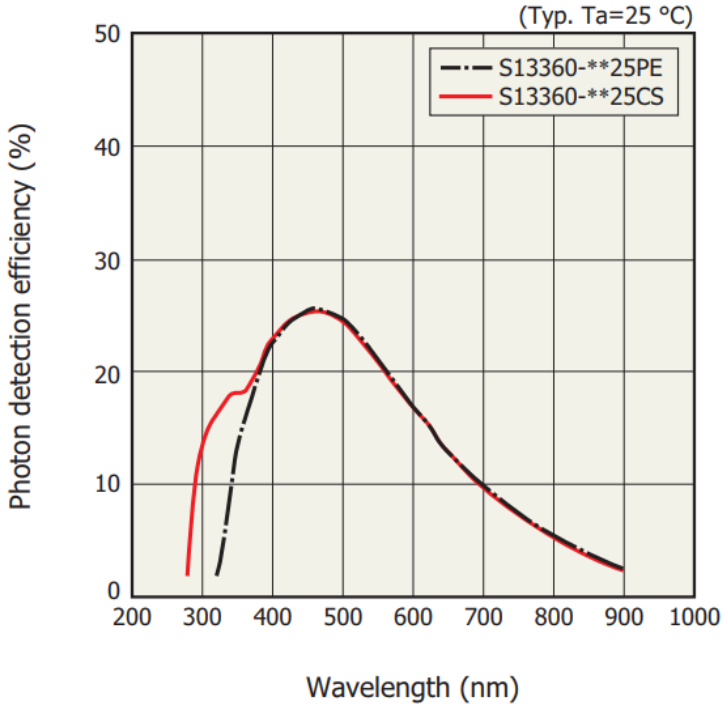

FIGURE 4.5: Photon detection efficiency of the MPPC vs wavelength.

4.2 Positioning

The scintillation detector system for Phase 2 and 3 consists of 40 scintillators around the QCS magnets. They are positioned in 10 z positions, each with one scintillator at 0°, 90°, 180°, and 270° in ϕ. The positions were picked to maximize sensitivity to backgrounds according to simulation and with regards to space constraints. The space where scintillators will be located is occupied by parts of the inner detectors, such as

cabling and cooling for the vertex detectors, as well as sensors monitoring the alignment of the QCS magnets relative to the Belle II detector.

The scintillators are strapped onto the QCS by two thin aluminum bands (0.3 mm height $\times$2 cm width) each. The aluminum bands are secured around the scintillator by two non-magnetic steel parts (with the purpose of keeping an uniform magnetic field inside the Belle II solenoid) designed to hold the scintillator in place and ensure the 90° bend angle of the aluminum band. The steel parts are held together by two bolts (made from brass - also non-magnetic). The drawing of one steel part is shown in Figure 4.6. This piece slides around the scintillator. The aluminum band is placed over the scintillator and the first metal piece, shown in Figure 4.7. Two of the bands are needed to create a full circle and so in total four will hold four scintillators. The last parts, shown in Figure 4.8, are placed on each side of the scintillator and secured with a bolt. These drawings were made in Inventor, a software used for mechanical design [29]. All dimensions are in mm and the color of the drawings is not representative of reality, it was chosen to distinguish between all parts.

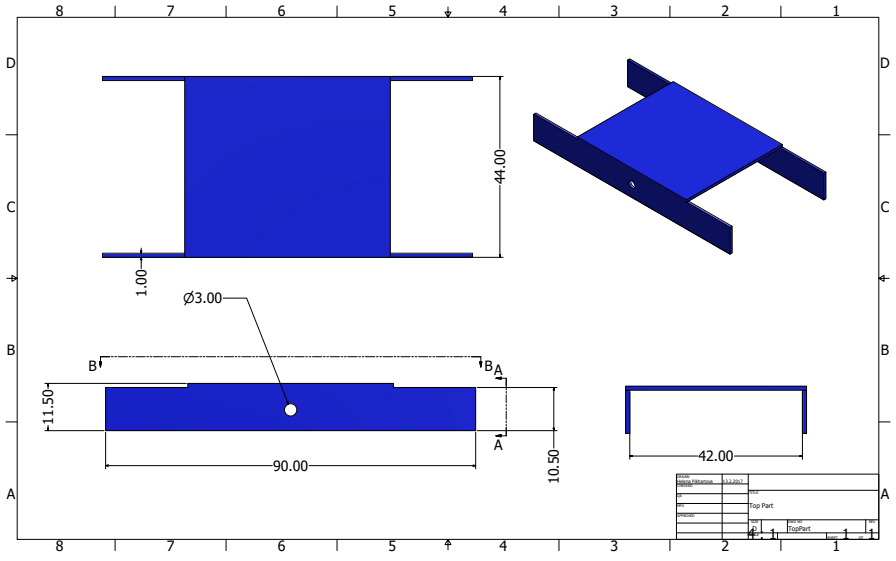

FIGURE 4.6: Non-magnetic steel part surrounding scintillator.

A complete model of the attachment with cables is shown in Figure 4.9. The cables chosen for this setup are Cat7, an ethernet cable including four twisted pairs of copper wires with plastic shielding. Each cable connects 4 scintillators, so the total number of cables needed is 10. The cables will be attached to the point where the aluminum bands are connected together, at 45° angle in ϕ, relative to the scintillators, with cable

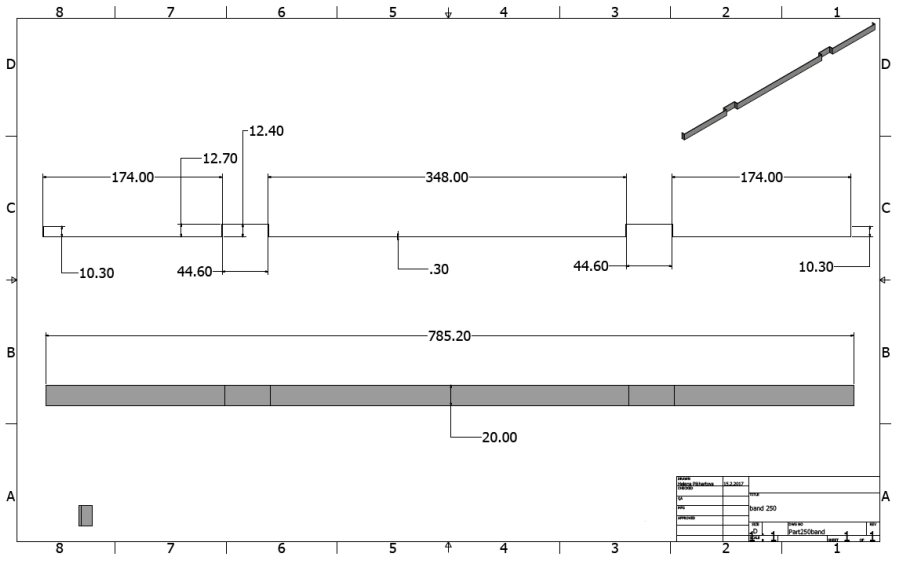

FIGURE 4.7: Aluminum belt strapping the scintillators onto the QCS. Two of these are connected together to form a circle around the QCS. Four together hold four scintillators.

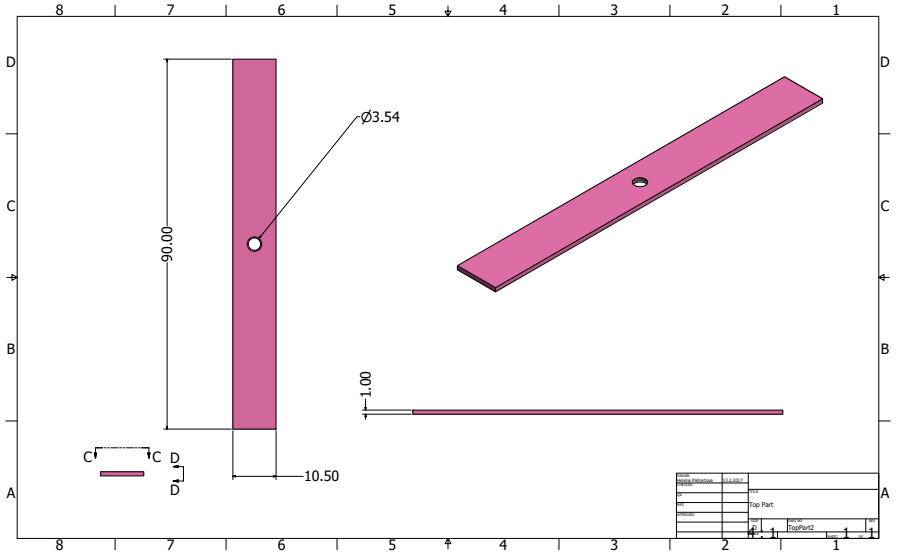

FIGURE 4.8: Top part holding scintillator with a tap hole for a bolt. Two of these are necessary for one scintillator.

fasteners. The Cat7 cables are able to work at transmission frequencies up to 600 MHz [30], which is compatible with the projected background rates from simulation.

The positions relative to the QCS are shown in Figure 4.10. The figure shows a cross section through the QCS structure in the xz plane, showing the inner layers, including the beam pipes and the focusing magnets. Different colors represent the cumulative radiation length traversed by a particle traveling through a thin x-z slice. Denser material

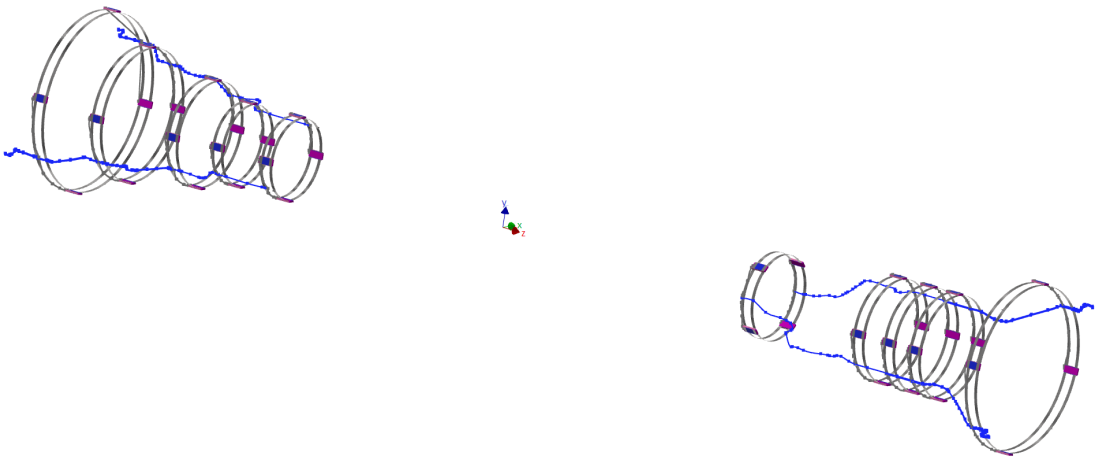

FIGURE 4.9: 3D model of scintillator attachment with cables. The gray circles show the aluminum bands holding the scintillators (in pink) in place together with metal pieces (in blue); cables are shown in blue on two sides of the structure. The cable shape mimics the QCS surface.

has lighter colors (i.e. tungsten shields are shown in yellow). The scintillators have been implemented in the Geant4 detector geometry simulation used by the Belle II collaboration. The results of studies using this simulation are presented in Chapter 5.

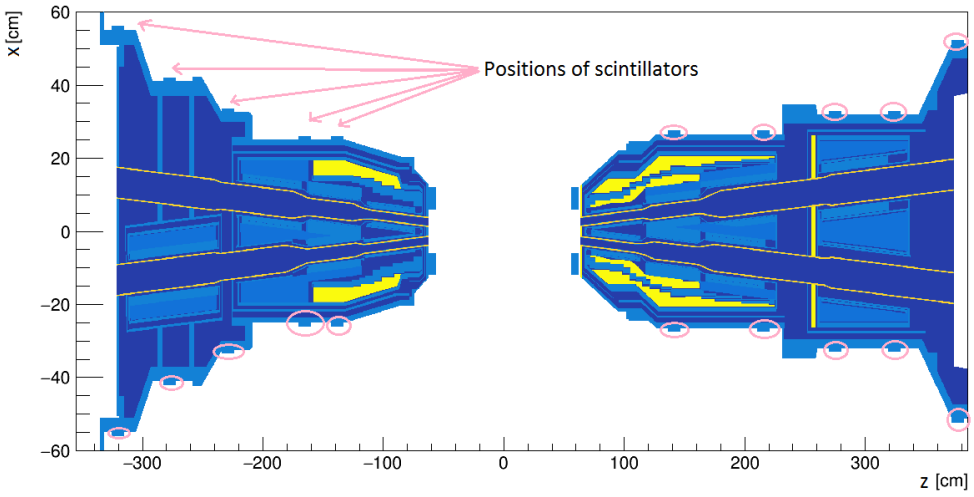

FIGURE 4.10: Material scan of QCS structure showing scintillators in position by arrows and circles. Only the scintillators at $\phi = 0, \pi$ radians are visible. Material scan shows the different components with distinct density.

A test installation of one attachment structure was done in March 2017 (Figure 4.11). The test successfully validated the attachment design.

FIGURE 4.11: Test installation of one attachment structure with scintillators on QCS right.

4.3 Readout

Each MPPC produces electric current in response to beam background events which is read out in the data acquisition room, near the detector space. The front-end part of the readout is done by an EASIROC board. The EASIROC module is a special ASIC NIM board [31] developed by Omega/IN2P3 in France [32]. It has many functions such as amplifier, shaper, discriminator and voltage supply for each MPPC. Each board can support 32 signal channels.

The optimal plan is to have two EASIROC boards, one in the backward and one in the forward direction (simplified diagram shown in Figure 4.13), each of them handling the readout for 20 scintillators. The cable length between the sensors and the DAQ room will be around 30 m. Each EASIROC board will be connected to a picoscope for live waveform analysis and then output into a computer. The picoscope is a PC based oscilloscope; a cheaper and smaller version of a desktop oscilloscope. The computer will operate the picoscope and EASIROC software, and pass the results to the SuperKEKB and Belle II control rooms. Results will include hit rates of beam backgrounds detected by each scintillator. The picoscope will be used for monitoring the waveform of a single channel, which will be used to control the operation of the MPPCs and the EASIROC board.

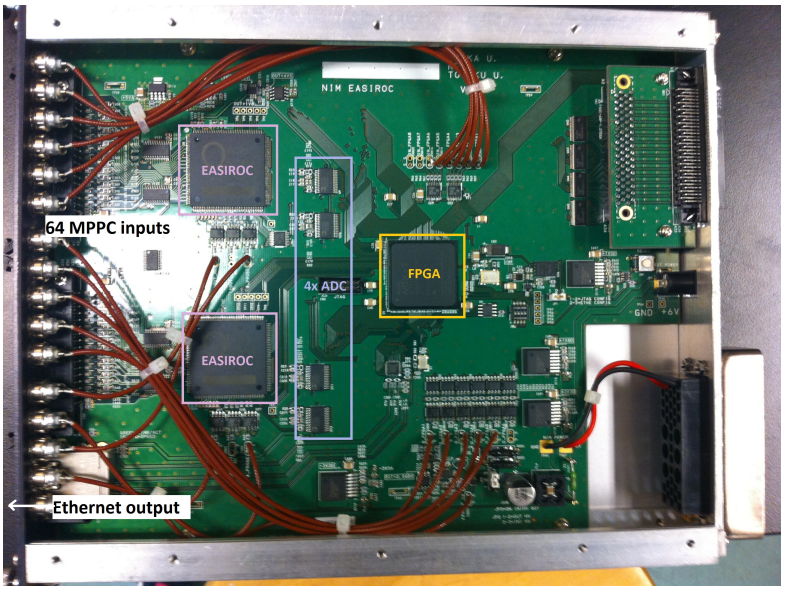

FIGURE 4.12: Photo of an EASIROC NIM board used for readout with highlighted main components.

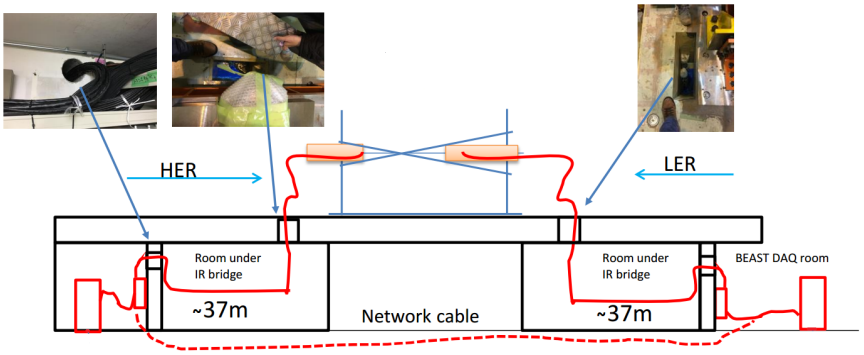

FIGURE 4.13: Simplified diagram of the readout path with images of gaps where cabling passes from one room to another.

4.3.1 EASIROC

The EASIROC (Extended Analogue SiPM Integrated Read Out Chip) board is composed of a system of readout electronics: the 64 channel MPPC inputs, the EASIROC chip, ADCs, FPGA and TDCs; which are presented in this section. An image is shown in Figure 4.12.

Each MPPC input is processed separately by the EASIROC chip (Diagram in Figure 4.14). The gain of each MPPC input can be adjusted by varying the input DAC voltage ($0-4$V). The signal goes through two amplifiers (low gain and high gain, with a factor of 10 between these two) and is shaped by slow and fast shapers to deliver the measurement of charge and timing (shaping times 50 and 175 ns respectively). The Channel0_trigger

output is used to implement the function for counting hits in the downstream FPGA. Individual discriminator outputs, analog outputs and bias adjustments are available for each channel. Each EASIROC chip is connected to two ADCs (for low gain and high gain). The FPGA has a MHTDC (multi-hit TDC) implemented with timing resolution of 460 ps [33].

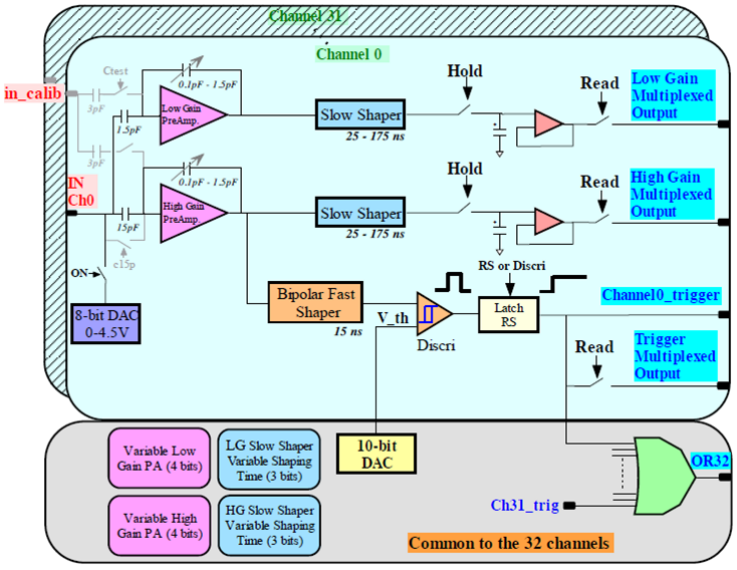

FIGURE 4.14: One of two EASIROC chips present on each board. Each chip handles 32 inputs and provides pre-amplifiers, slow and fast shapers and amplifiers.

The board generates trigger and hold signals internally. An example of a waveform is shown in Figure 4.15. This was recorded during cosmic radiation testing at McGill. The top waveform (pink) shows the trigger window generated by the EASIROC board and the bottom waveform (yellow) shows the analog output of the MPPC. The output is provided with internal delay such that the maximum of the signal coincides with the trigger. The data collection is done in an approximately 4 μs window with 320 ns collection time.

4.3.2 DAQ

During Phase 2 running, data acquisition for the scintillator sensors will be effected by the centralized system of all BEAST II detectors. The software used for this purpose is the Experimental Physics and Industrial Control System (EPICS) [34]. This software is designed to provide control and feedback for systems handling large numbers of networked computers.

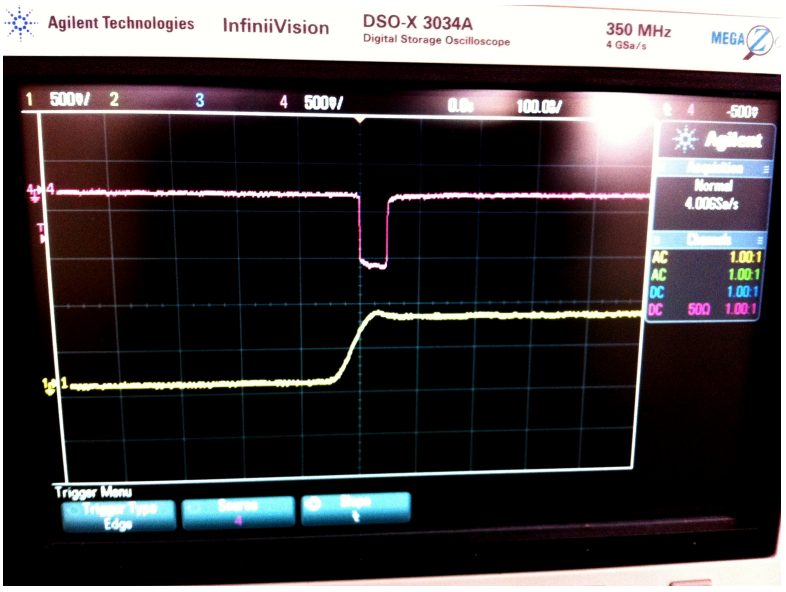

FIGURE 4.15: Oscilloscope screen showing trigger and MPPC analog output wave form. The time scale is 100 ns per division.

The feedback strategy is to provide results (sum of hits for each scintillator) at 1 Hz frequency for analysis. This will allow for monitoring average rates per scintillator and observing unwanted fluctuations. It is anticipated that accelerator operators can use these signals for real-time tuning of the beam conditions. In addition, all collected data will be stored for an off-line analysis.

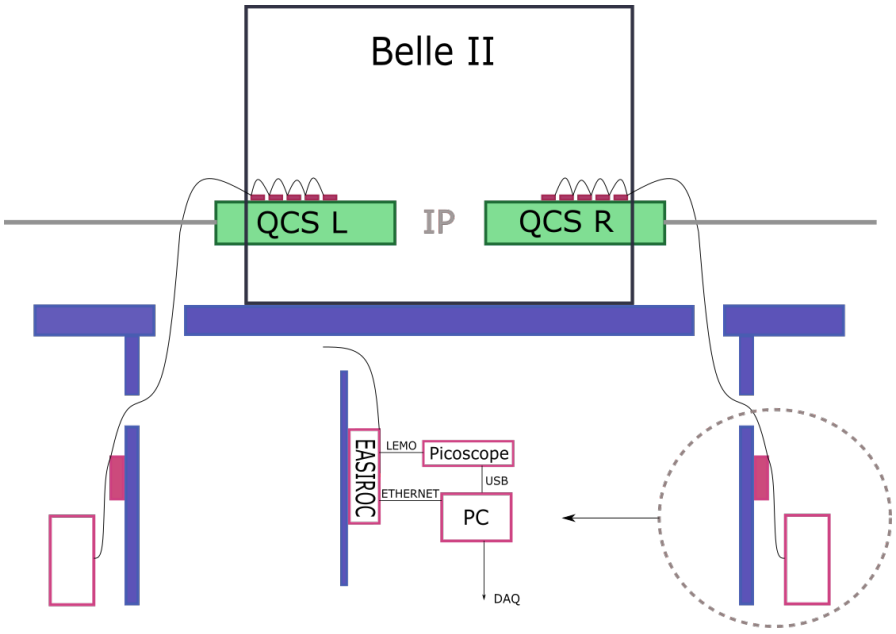

FIGURE 4.16: Simplified diagram of the readout path showing scintillators on top of the QCSs connected to the readout in the specific DAQ rooms and a detail of readout setup (EASIROC board, picoscope and PC).

Chapter 5

Beam Background Simulation

Beam background simulation is a very important tool for safe and smooth operation of SuperKEKB and Belle II. For this project, it enables imaging the system of scintillators around the QCS volume. The cross section of the QCS with scintillators attached is shown in Figure 4.10. The simulation was specifically used for choosing the exact positions of scintillators and predicting the background rate for each of them.

The structure of the accelerator in the vicinity of the interaction point is very important, i.e. the beam pipe diameter decreases before the IP and then increases, which affects the distribution of background hits. Looking at the plot in Figure 3.4, the electron beam (HER) enters the QCS from the backward side through the pipe at negative x and exits through the forward side at positive x. The positron beam (LER) approaches the IR from the forward side at negative x and exits the backward side at positive x.

5.1 Tools

There are different tools handling the beam background simulation used within the Belle II software framework, *Basf2* [35]. Geant4 [36] is a simulation package that is used for simulating particle propagation and interactions within the IR region and detector. The information about particle trajectory and energy is delivered to Geant4 from event generators. These generators are specific for each background source. Touschek and Beam-Gas radiation are generated using the SAD software [37], synchrotron radiation is done using a single particle generator in Geant4 and radiative Bhabha background is

simulated with BBBrem [38] and BHWide [39] generators. The injection background is not currently simulated but it is planned to be done with SAD.

5.1.1 Geant4

Geant4 is the software simulating the passage of particles through matter [36]. It handles the simulation of particle interactions and shower development when the SAD places loss positions near the interaction point. After the simulation, the interactions and showers are manually weighted based on material characteristics and the accelerator parameters (structure of movable collimators near the IP, vacuum pressure for beam-gas interactions) at the point of interaction. Similar processes occur for the generators BBBREM and BHWide, after the particles intersect with the detector volume. Also the Belle II detector is modeled within the Geant4 software including information about dimensions and material of each subdetector.

5.1.2 SAD

The software used for propagating particles through the simulated accelerator lattice is the Strategic Accelerator Design (SAD) [37]. It is employed on the full accelerator lattice. SAD generates energy or angular scattering events in each ring section and propagates the resulting particles through the lattice to the region of the IP. Once the scattered particles hit the machine aperture, SAD records information about their energy loss and position. If the simulated particles reach the Belle II detector volume, the simulation is handed to Geant4 tools. For Belle II, the SAD estimates beam loss rates from beam-gas and Touschek scattering processes.

5.1.3 Bhabha scattering generators

Two generators, BBBREM [38] and BHWide [39], are used to simulate the background created by Bhabha scattering. They both use Monte Carlo algorithms to generate events with characteristic initial conditions. BBBREM serves to simulate Bhabha background at low scattering angle while BHWide is used for Bhabha radiation with large angle scattering ($\theta > 0.5$ radians). The results of the two generators are combined in order to correctly represent the entire phase space for Bhabha events. Kinematic cuts are

imposed on each generator to ensure that there is no overlap between the two generators. The two samples are independently scaled according to their respective cross sections to correspond to equivalent integrated luminosities, i.e. data taking times.

5.2 Position Simulation

Beam background is position dependent which influences the choice of positioning of scintillator sensors. The primary hit positions of the incident background particles at the design luminosity for different background sources are shown in Figure 5.1. The x axis represents the loss position, more specifically the position where the background particle hits the beam pipe. The arrows project the direction of propagation of the background particles as they enter the detector volume.

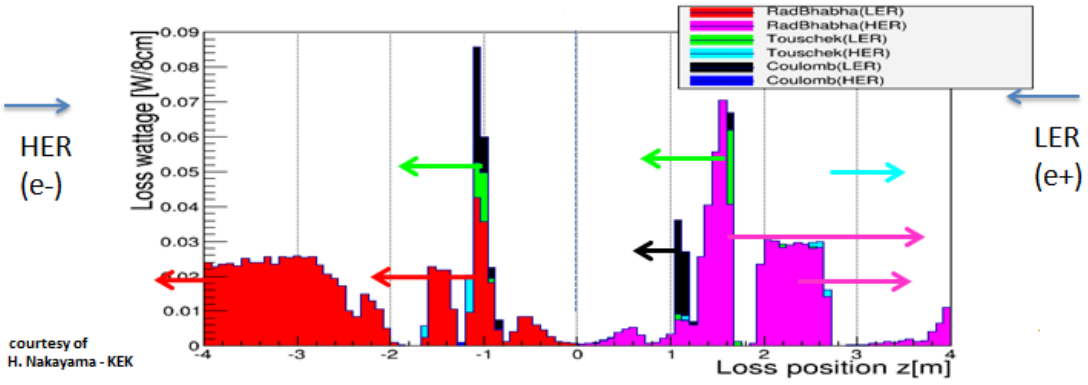

FIGURE 5.1: Simulation of the beam loss near the interaction point due to beam backgrounds with Phase 3 conditions.

The positions of the scintillator sensors were determined using simulation. In this case, the outer-most layer of QCS was used as a sensitive detector in the Geant4 simulation to represent the background rate at the proposed location of the scintillators. The places with the highest concentration of background hits were selected as the best candidates for the positions of scintillators. However, the final decision was made based on physical constraints from other structures on the surface of QCSs, for example cables, not all of which are fully modeled in the Geant4 simulation model. The highest concentration of the beam background hits will ensure the lowest statistical error. A detector located at a lower concentration might not observe changes to the background rates if they are within the uncertainties. The whole system of 40 detectors at different locations will provide an information of relative changes in background types.

The simulation was performed for background created by Coulomb, Touschek and Bhabha scattering. Coulomb and Touschek backgrounds are divided by ring of origin (Low Energy Ring or High Energy Ring) and Bhabha is separated by the two generators (BBBREM and BHWide, with applied cuts to ensure no double counting of background events). 2D histograms were created by projecting the z coordinate in cm onto the histogram x-axis and ϕ coordinate in radians onto the y-axis. $\phi = 0$ corresponds to x = 0, which is the inner side of the ring, $\phi = \pi/2$ is the top of the beam pipe, $\phi = \pi$ is the outside of the ring and $\phi = 3\pi/2$ is the bottom of the beam pipe. The z-axis represents the raw number of hits per one background event.

Figure 5.2 shows the distribution of background hits created by Coulomb radiation on the surface of the QCS structure. The plots show the hit distribution on the QCS, with x axis as the z position and y axis the ϕ angle. The Coulomb background distribution is created with 1×10^{-4} s sample (the equivalent time of the raw simulated sample) using design accelerator conditions for Phase 3 (pressure in the order of 10^{-7} Pa, beam currents $I_{HER} = 2.62$ A and $I_{LER} = 3.60$ A [18]) - the simulated sample has the statistics equivalent to running SuperKEKB at nominal design operating conditions for 10^{-4} s. The majority of the Coulomb background is created by the LER beam (the positrons). The LER has a higher hit structure between z = $[-335, -210]$ cm (QCS location under the backward side of KLM), centered around the inside of the ring ($\phi = 0$). A higher concentration of hits is also located around z = $[-100, -60]$ cm (QCS location under the pre-amplifiers of the CDC). The HER has the highest concentration of background hits between z = $[-90, -50]$ cm (also under CDC pre-amplifiers), and in this case, the hits are centered on the outside of the ring (around $\phi = \pi$).

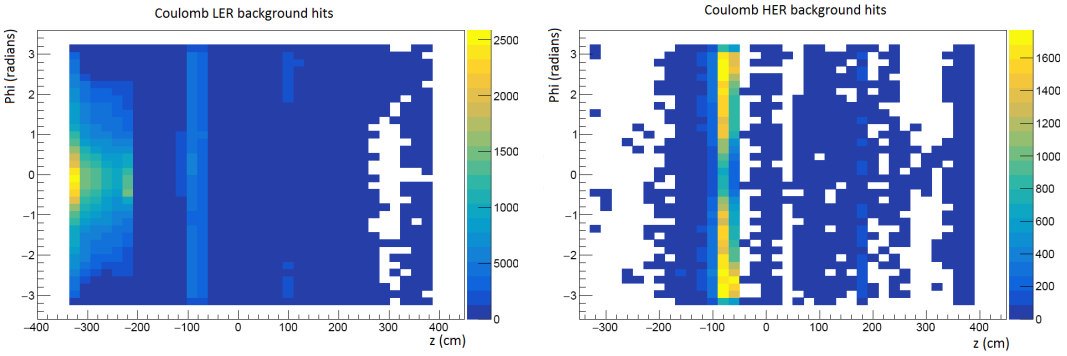

FIGURE 5.2: Background hits created by Coulomb scattering on the outermost layer of QCSs for LER and HER. Distribution shown for z and ϕ coordinate with color scheme corresponding to different number of hits for each bin.

The distribution of Touschek background hits is shown in Figure 5.3. The LER contribution is again higher than HER. LER hits are located between z = $[-335, -200]$ cm with most at $\phi = 0$. Most HER hits are located at z = $[-100, -60]$ cm with $\phi = \pi$ and at z = $[340, 380]$ cm (QCS location under the forward side of KLM) with $\phi = 0$. Touschek background hits were collected during time of 1×10^{-4} s (with Phase 3 conditions).

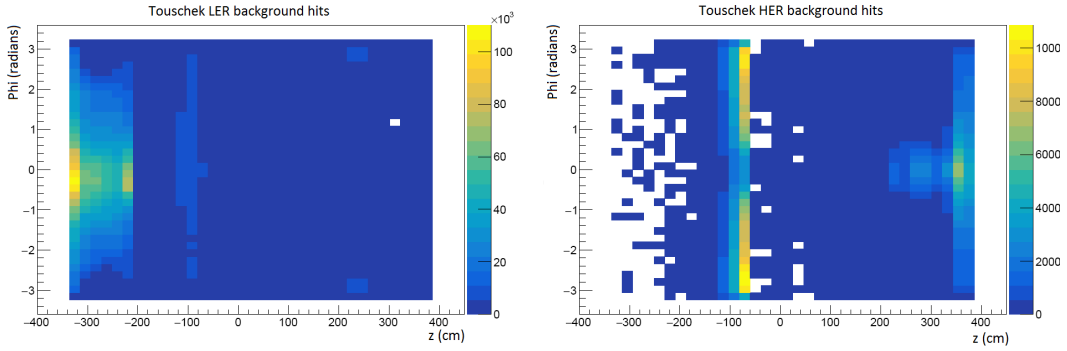

FIGURE 5.3: Background hits created by Touschek effect on the outer most layer of QCSs for LER and HER. Distribution shown for z and ϕ coordinate with color scheme corresponding to different number of hits for each bin.

The Coulomb and Touschek backgrounds show similar patterns. The LER beam has a higher concentration of background hits in the downstream part (after passing through the IP) centered at $\phi = 0$ radians (x coordinate positive, y coordinate = 0). This can be explained by the fact that the beam pipe is moving away in the horizontal plane from x = 0 to x = 15 cm within the length of the QCS left. As the beam is pushed towards positive x, the beam background appears in higher concentration in this direction. In this direction, the background needs to pass through less QCS volume and therefore less background is absorbed before hitting the outermost layer of QCS. The HER beam shows higher concentration of background hits in the upstream part (before reaching the IR). The hits are centered around $\phi = \pi$ radians which corresponds to the outside of the ring (negative x axis) on the horizontal plane (y = 0). Since the beam pipe is coming closer towards the center of the QCS (towards x = 0) before the IR, more background hits the sides at this point. In general, QCS left has less tungsten shielding, smaller radius before |z|= 200 and less material within its radius after |z|= 200 (Figure 4.10), therefore more background propagates through its volume.

Radiative Bhabha background simulated using the generators BHWide and BBBrem are shown in Figure 5.4. The plots display the number of background hits per one event (scale shown on z axis) on the QCS outermost layer (z by ϕ). The background hits for

wide angle Bhabha radiation are based at z = $[-100, -60]$ cm with $\phi = -0.6$. The data sample for BHWide is 1×10^{-3} s. Small angle radiative Bhabha background hits are located at z = $[-335, -200]$and $[220, 260]$ cm (the second interval is located under the boundary between ECL and KLM on the forward side) with the highest rate occurring at $\phi = 0$ and also at $[-100, -80]$ cm with $\phi = -0.6$. The data sample of BBBrem is also 1×10^{-3} s (scaled sample to correspond to the BHWide data sample). Both samples taken at Phase 3 conditions with instantaneous luminosity of 8×10^{35} cm^{-2} s^{-1} [18]. It is noticeable that small angle radiative Bhabha (BBBrem generator) is the most dominant background source.

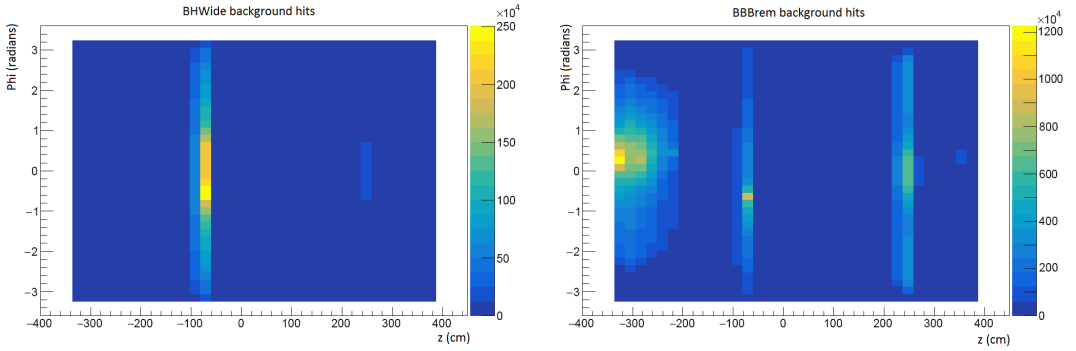

FIGURE 5.4: Background hits created by Bhabha scattering on the outer-most layer of QCSs with its wide angle Bhabha and small angle Bhabha scattering components. Distribution shown for z and ϕ coordinate with color scheme corresponding to different number of hits for each bin.

Radiative Bhabha background hits plots are created from a joint data sample of both LER and HER particles.

The preferred positions are not all accessible as the QCS surface provides other functions. There are gap sensors to monitor the distance from the QCS to the detector, laser tracker systems and tap holes. These are shown in Figure 5.5 in red. In addition, Figure 5.6 shows a vacuum connection mechanism, which is attached to the QCSs and takes space from -1451 to 2178 mm in z. It is therefore impossible to attach any scintillators in this region at the 0° and 180° in ϕ.

Using this simulation and QCS space constraints, the positions of the scintillators are summarized in Table 5.1. In most cases, a z position has been selected with four sensors placed at $\{0, 90, 180, 270\}$° in ϕ except in three instances in which sensor positions are rotated by 6 to 15 degrees to avoid the RVC structure and laser tracker holes.

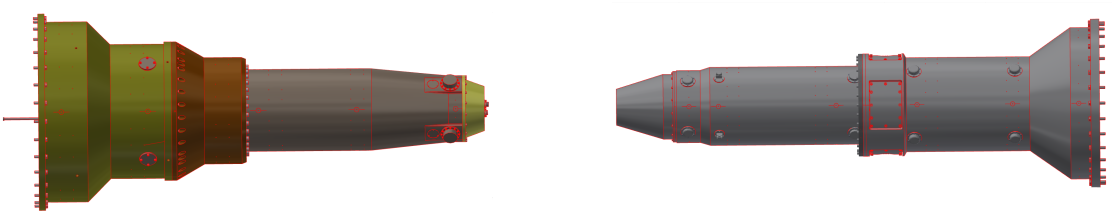

FIGURE 5.5: QCS Left and Right with surface structures (in red) which are not allowed to be covered with any material.

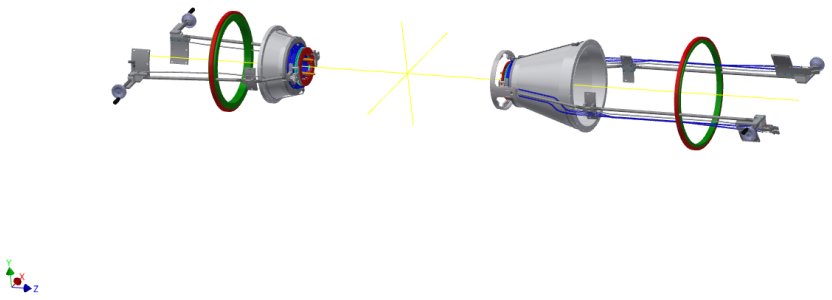

FIGURE 5.6: Remote vacuum connection (RVC) mechanism providing vacuum for the beam pipes in the vicinity of IP.

z (cm)	−312	−279	−229	−201	−165	192.8	279.3	302	321.1	377.1
angle (°)	6 96 186 276	0 90 180 270	0 90 180 270	0 90 180 270	0 90 180 270	15 105 195 285	0 90 180 270	0 90 180 270	0 90 180 270	6 96 186 276
ring number	−5	−4	−3	−2	−1	1	2	3	4	5

TABLE 5.1: Summary of scintillator positions around the QCS (point at the center of the scintillator volume). Ring number is used as an identification.

The highest background rates are in general located at $\phi = 0°$ and 180°, however scintillators are also positioned at $\phi = 90°$ and 270° in order to help differentiate background contributions from various sources, as discussed in the following sections.

5.3 Rate Simulation

After the positions were picked using the method described in the previous section, the scintillators were added to the Geant4 simulation of the detector volume (simulated scintillators around QCS left are shown in Figure 5.7). For the purposes of the simulation, only the scintillator material (without MPPC and attachment structure) was used. The simulation determines how many particles pass through the scintillating material and deposit energy. The material used in the Geant4 software is vinyl-toluene based scintillator (chemical structure - C_9H_{10}) with density $\rho = 1.032$ g/cm^3. All simulation in this section is done using the design beam parameters and luminosity (conditions foreseen for advanced Phase 3 operation).

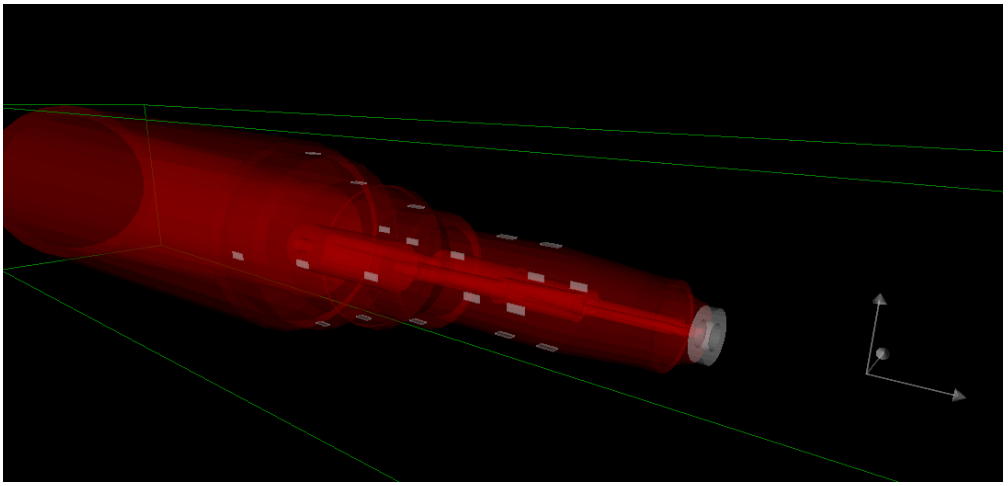

FIGURE 5.7: Scintillators (rectangular box of $4 \times 10 \times 1$ cm^3) visible in white on top of the surface of QCS left in red.

Using the scintillators as sensitive detector volume, it is possible to simulate how much background the scintillators will obtain. The scintillators will record the number of hits during a fixed time interval. Since one particle can interact multiple times within the scintillator, it is necessary to integrate the number of individual hits per one event. This information is converted into a background hit rate for each scintillator. The rates of each scintillator are simulated and compared in Table 5.2. Each x bin represents one z position and each y bin is a ϕ angle $(0, 90, 180, 270)^\circ$(except the positions which are slightly rotated). The uncertainties represent the statistical errors of the simulation. It is noticeable that the highest background rates are located in the backward region and also mostly in the scintillators at 0°. The background can be divided into individual sources (Figure 5.8, with a 3D model showing where is each scintillator located), where the

Touschek and Coulomb rates are shown for both LER and HER. BHWide and BBBrem include the sum of both LER and HER background. It is clearly visible that radiative Bhabha background will dominate the background recorded by the scintillators at design luminosity.

	-5	-4	-3	-2	-1	1	2	3	4	5
Bottom	0.7 ±0.2	7.2 ±0.5	17.9 ±0.8	18.1 ±0.9	6.6 ±0.5	1.1 ±0.2	0.7 ±0.2	1.3 ±0.3	0.4 ±0.1	1.5 ±0.3
Outside	0.4 ±0.1	0.9 ±0.2	3.1 ±0.3	0.9 ±0.2	1.2 ±0.2	0.9 ±0.2	0.6 ±0.2	1.4 ±0.2	0.1 ±0.1	0.5 ±0.2
Top	10.4 ±0.5	7.0 ±0.5	22.6 ±1.0	25.3 ±1.1	7.9 ±0.6	1.5 ±0.2	0.7 ±0.2	1.7 ±0.3	0.3 ±0.1	1.3 ±0.2
Inside	6.0 ±0.4	14.7 ±0.7	34.6 ±1.2	59.1 ±1.7	17.1 ±0.9	1.1 ±0.2	4.9 ±0.5	11.3 ±0.7	3.1 ±0.4	3.0 ±0.4

TABLE 5.2: Background rates (in MHz) recorded by each scintillator as a function of position (5 backward positions and 5 forward positions along the QCSs) and ϕ positions relative to the SuperKEKB rings (bottom, outside, top, inside) using Phase 3 conditions.

Figure 5.9 shows individual background rates by the z position of the scintillator. Each plot shows the rates divided into different ϕ position by line color. Integrating over the ϕ angles and placing all background sources together, background can be sorted by the z position (Figure 5.10).

The rates predicted by simulation are compatible with the performance of the scintillator sensors. The readout supports results of the order of $\sim 10^8$ Hz while the simulation predicts maximum rates of $\sim 10^7$Hz.

The results of Phase 1 have shown that the simulation can predict absolute rates only to within an order of magnitude for various detectors, but obtains the correct trends in terms of sensitivity to beam currents, beam size and angular distributions [24].

5.3.1 Phase 2 simulation

During Phase 2, the luminosity will be a factor of 40 lower than during Phase 3 operation. Luminosity dependent background will therefore be decreased significantly. Figure 5.11 shows rates of each background source with Bhabha radiation scaled by 1/40. A luminosity decrease implies lower beam parameters such as currents or bunch densities. This will also affect Touschek and beam-gas contributions. As Phase 2 beam conditions are not yet perfectly known, it is not possible to make accurate simulations. However it

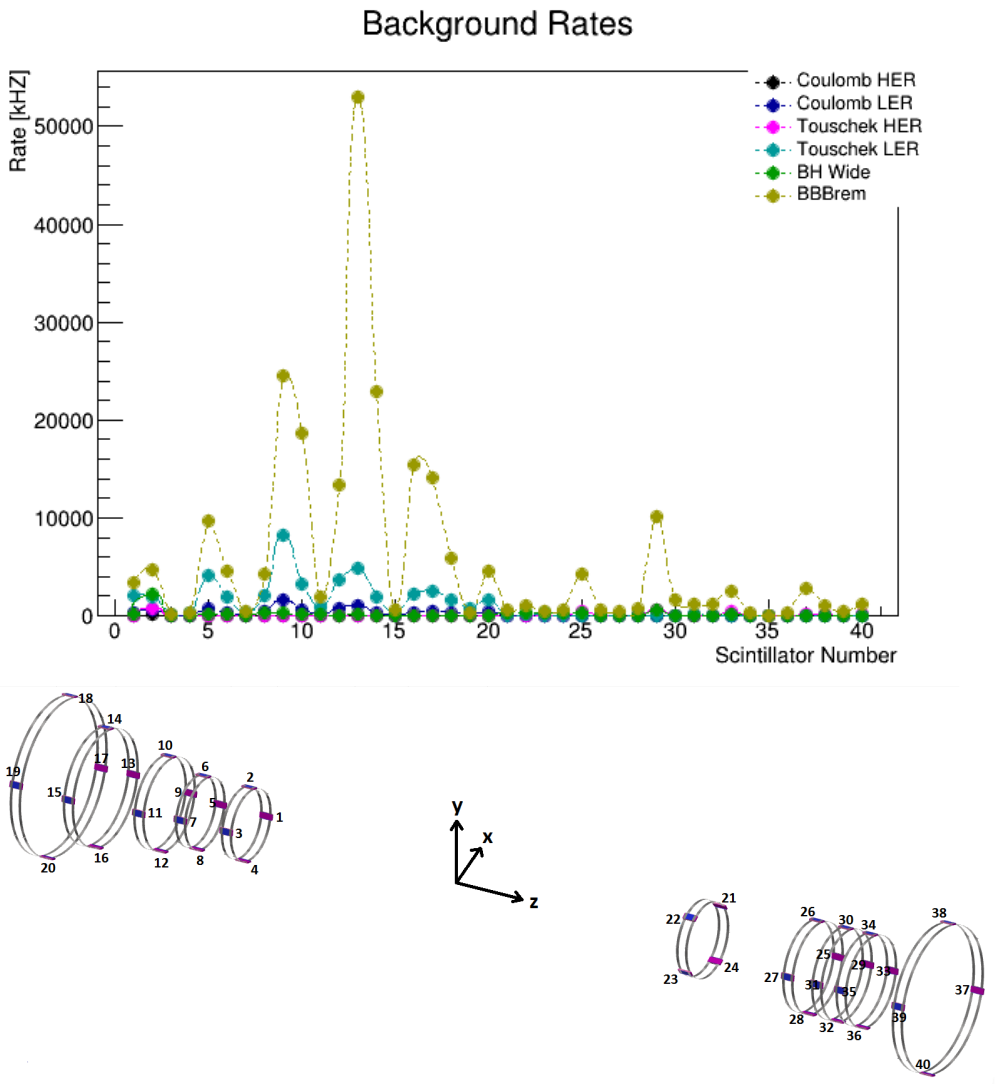

FIGURE 5.8: Individual background rates recorded by each scintillator. Each integer (1 - 40) corresponds to one scintillator. Each position is projected onto a 3D model of scintillators in the bottom image.

can be concluded that the scintillator beam monitors will be sensitive to different sources than just luminosity dependent backgrounds.

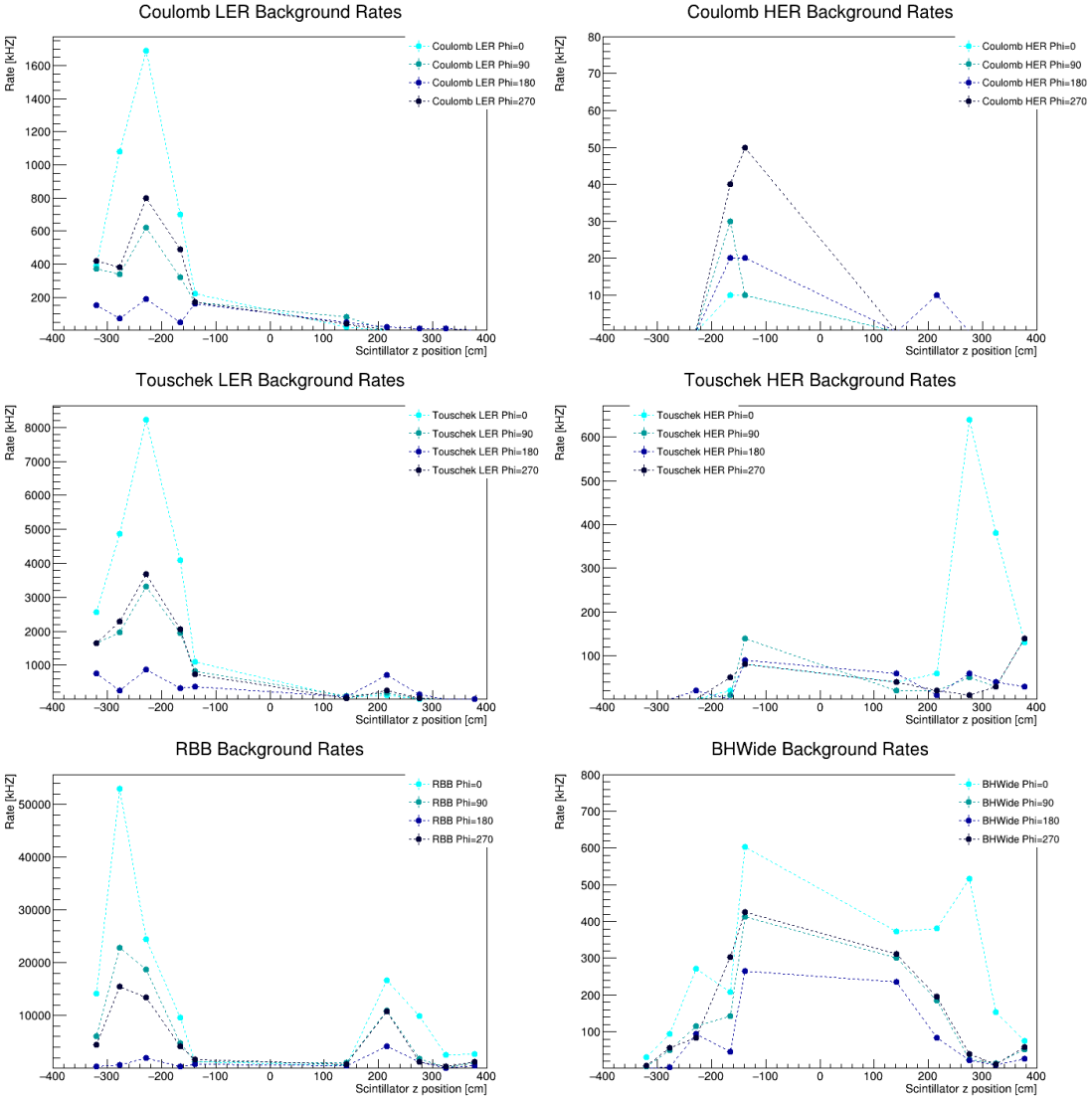

FIGURE 5.9: Individual background rates by background types (Coulomb LER and HER, Touschek LER and HER, Bhabha for low and wide angle) as a function of z position. Individual lines represent different ϕ position.

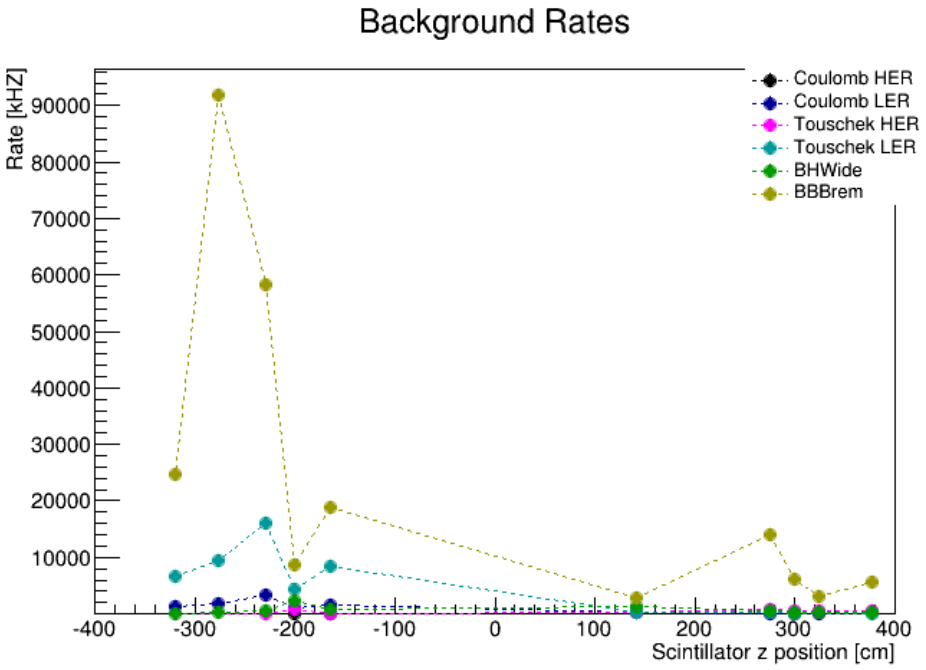

FIGURE 5.10: Background rates recorded by each scintillator for individual background sources integrated over all ϕ angles to show background dependence on z position.

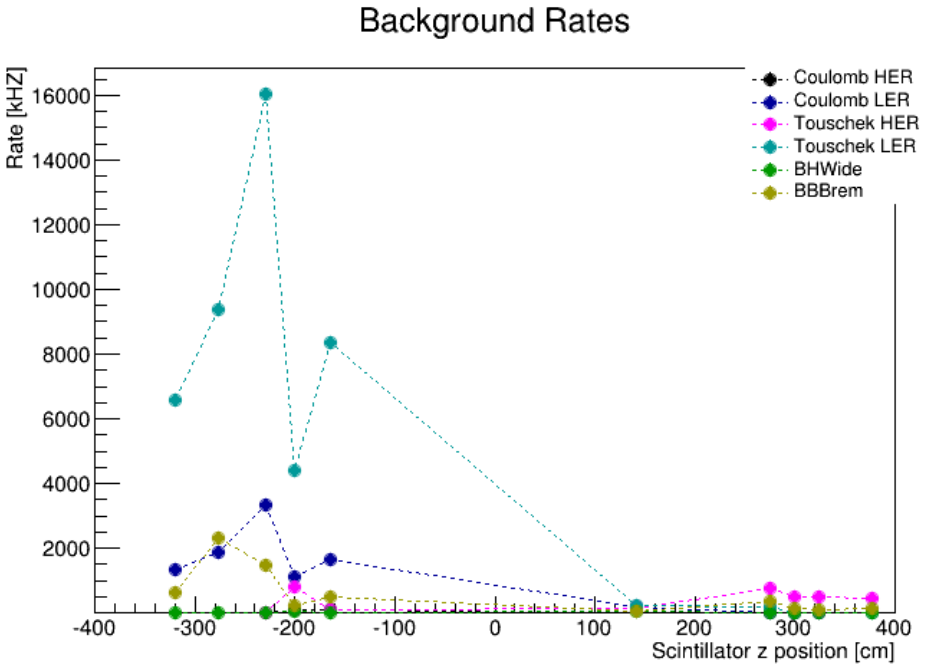

FIGURE 5.11: Background rates scaled for Phase 2 operation recorded by each scintillator for individual background sources integrated over all ϕ angles to show background dependence on z position.

Chapter 6

Discussion and outlook

The scintillator monitors need to be ready for full installation in autumn of 2017 and the beginning of Phase 2 in February 2018. The objective of this thesis project is completed, but there are other items which will be done after submission of the thesis by others.

Production of attachment pieces will begin soon so as to collect all necessary parts before installation. This includes the aluminum and metal parts described in Chapter 4, as well as purchase of the cables. Additional testing of cables is necessary to ensure low noise while keeping the diameter of the cable small enough to access the detector. In addition, all parts have to be low smoke, zero halogen and non-magnetic.

The software for monitoring and output needs to be incorporated into the EPICS system within the BEAST II working group. This will allow the output to be monitored in the Belle II and SuperKEKB control rooms. Additional software needs to be implemented to provide monitoring of the whole system (scintillator operation, software controls). This work is currently in progress.

Installation of the beam monitor hardware is anticipated to take place during the fall of 2017. Details of full installation need to be coordinated with other sub detector groups, which use the space around QCS for cabling and gas/cooling pipes. At the time of installation, all pieces have to be assembled at the detector site and the installation plan has to be carefully coordinated with other detector assembly and operations schedules. This includes processes such as cable attachment and wire to scintillator bond procedure step by step plan. After installation, the whole setup will stay in place until the beginning of Phase 2. In the case of malfunction of one scintillator MPPC, the rest of the system

would be unaffected. An exchange of such a broken piece might not be possible until the end of the Phase 2 run. If an EASIROC board were to break, the whole forward or backward region would be affected. The replacement of a malfunctioning board could be done during the months of operation as these are located off-detector in the data acquisition room.

Chapter 7

Conclusion

This thesis presented the design of a system of scintillator detectors with the purpose of monitoring beam background at the Belle II detector. Work presented describes the scintillators, readout and simulation.

The scintillator detectors monitor background by recording rates of particles interacting within their volume. These interactions come from background particles hitting the beam pipe and traveling through the QCS material. It is important to monitor this background as it negatively affects the detector through increasing occupancy and creating radiation damage to sensitive material. It also affects the signal to noise ratio of physics analyses.

The scintillators are positioned around the final focusing magnets at the positions of z $= \{-3120, -2790, -2290, -2010, -1650, 1928, 2793, 3020, 3211, 3771\}$ mm. Each z position has one scintillator at $\phi = \{0, 90, 180, 270\}^\circ$ or rotated by $6 - 15^\circ$in a few instances due to the presence of obstructions in the preferred positions. Each scintillator has a sensitive volume of 40 cm^3 and is coupled to a MPPC. Readout is done by 2 EASIROC boards, one on the backward side and one on the forward side of the Belle II detector. Online monitoring of rates recorded by the scintillators will be available in the control room of the SuperKEKB accelerator and the Belle II detector. The simulation shows that the most prominent background recorded by the scintillators will be radiative Bhabha during nominal phase 3 high-luminosity running, but during lower-luminosity commissioning will be dominated by the Touschek and Coulomb radiation. The background has a characteristic spatial distribution, which enables identification of more distressed positions. The simulated rates are in the range of kHZ to MHz for each scintillator.

The scintillators will be present in the Belle II detector during the final commissioning phase and the operation of the full detector. They are part of the BEAST II monitoring detector and will provide real-time monitoring information which enables optics parameters to be adjusted while running and hopefully improves the running of the Belle II experiment.

Bibliography

[1] Belle II experiment, 2017. URL https://www.belle2.org/.

[2] High energy accelerator research organization KEK. URL http://www.kek.jp/en/index.html.

[3] A. et al. Abashian. The Belle Detector. *Nucl. Instrum. Meth.*, A479:117–232, 2002. doi: 10.1016/S0168-9002(01)02013-7.

[4] Bernard et al. Aubert. The BaBar detector. *Nucl. Instrum. Meth.*, A479:1–116, 2002. doi: 10.1016/S0168-9002(01)02012-5.

[5] Nobelprize.org. The nobel prize in physics 2008. URL http://nobelprize.org/nobel_prizes/physics/laureates/2008/.

[6] D. N. Spergel et al. Three-year wilkinson microwave anisotropy probe (wmap) observations: Implications for cosmology. *The Astrophysical Journal Supplement Series*, 170(2):377, 2007. URL http://stacks.iop.org/0067-0049/170/i=2/a=377.

[7] Maarten C Brak. The hierarchy problem in the standard model and little higgs theories. 2004.

[8] C. et al. Patrignani. Review of Particle Physics. *Chin. Phys.*, C40(10):100001, 2016. doi: 10.1088/1674-1137/40/10/100001.

[9] Claus Grupen and Boris Shwartz. *Particle Detectors*. Cambridge University Press, second edition.

[10] A. Sommerfeld and H. Bethe. *Elektronentheorie der Metalle*, pages 333–622. Springer Berlin Heidelberg, Berlin, Heidelberg, 1933. ISBN 978-3-642-91116-3. doi: 10.1007/978-3-642-91116-3_3. URL http://dx.doi.org/10.1007/978-3-642-91116-3_3.

[11] Heitler Bethe and Walter Heitler. On the stopping of fast particles and on the creation of positive electrons. In *Proceedings of the Royal Society of London A: Mathematical, Physical and Engineering Sciences*, volume 146, pages 83–112. The Royal Society, 1934.

[12] S. Majewski, G. Charpak, A. Breskin, and G. Mikenberg. A thin multiwire chamber operating in the high multiplication mode. *Nuclear Instruments and Methods in Physics Research*, 217(1):265 – 271, 1983. ISSN 0167-5087. doi: http://dx.doi.org/10.1016/0167-5087(83)90146-1. URL http://www.sciencedirect.com/science/article/pii/0167508783901461.

[13] Lucien Pages, Evelyne Bertel, Henri Joffre, and Laodamas Sklavenitis. Energy loss, range, and bremsstrahlung yield for 10-kev to 100-mev electrons in various elements and chemical compounds. *Atomic Data and Nuclear Data Tables*, 4:1 – 27, 1972. ISSN 0092-640X. doi: http://dx.doi.org/10.1016/S0092-640X(72)80002-0. URL http://www.sciencedirect.com/science/article/pii/S0092640X72800020.

[14] I. J. H. Hubbell, H. A. Gimm. *Pair, Triplet, and Total Atomic Cross Sections (and Mass Attenuation Coefficients) for* 1 *MeV*–100 *GeV Photons in Elements* $Z = 1$ *to* 100. J. Phys. Chem. Ref. Data 9.

[15] Albert Einstein. The photoelectric effect. *Ann. Phys*, 17(132):4, 1905.

[16] Malcom J Cooper. Compton scattering and electron momentum determination. *Reports on Progress in Physics*, 48(4):415, 1985.

[17] Yung-Su Tsai. Pair production and bremsstrahlung of charged leptons. *Reviews of Modern Physics*, 46(4):815, 1974.

[18] T. Abe et al. Belle II technical design report. 2010.

[19] H. Bruck. *Circular Particle Accelerators*. LA-TR. Los Alamos Scientific Laboratory, 1972. URL https://books.google.ca/books?id=CXCqHAAACAAJ.

[20] William A. McKinley and Herman Feshbach. The coulomb scattering of relativistic electrons by nuclei. *Phys. Rev.*, 74:1759–1763, Dec 1948. doi: 10.1103/PhysRev.74.1759. URL http://link.aps.org/doi/10.1103/PhysRev.74.1759.

[21] M. Kikuchi et al. Design of positron damping ring for super-kekb. In *Proceedings of IPAC*, 2010.

[22] Yukiyoshi et al. Ohnishi. Accelerator design at superkekb. *Progress of Theoretical and Experimental Physics*, 2013(3), 2013. doi: 10.1093/ptep/pts083. URL http://ptep.oxfordjournals.org/content/2013/3/03A011.abstract.

[23] Weiren Chou Alexander W Chao. *Reviews of Accelerator Science and Technology: Volume 7: Colliders*. World Scientific.

[24] BEAST II Collaboration. First Measurements of Beam Backgrounds at SuperKEKB. *to be submitted to NIMA (2017)*.

[25] H Nakayama, Y Funakoshi, Y Onishi, K Kanazawa, and T Ishibashi. Superkekb background simulation, including issues for detector shielding. *Energy [GeV]*, 3:8–0.

[26] Yukiyoshi et al. Ohnishi. Accelerator design at superKEKB. *Progress of Theoretical and Experimental Physics*, 2013(3):03A011, 2013. doi: 10.1093/ptep/pts083. URL http://dx.doi.org/10.1093/ptep/pts083.

[27] Hamamatsu photonics K.K. URL http://www.hamamatsu.com/jp/en/S12572-025C.html.

[28] HAMAMATSU PHOTONICS K.K. Solid State Division. *MPPC (Multi-Pixel Photon Counter)*. URL http://www.hamamatsu.com/resources/pdf/ssd/s13360_series_kapd1052e.pdf.

[29] Autodesk inventor. URL http://www.autodesk.ca/en/products/inventor/overview.

[30] Allan Nielsen. *AMP NETCONNECT Guide to ISO/IEC 11801 2nd Edition Including Amendment 1*.

[31] S. Callier, C. D. Taille, G. Martin-Chassard, and L. Raux. EASIROC, an Easy & Versatile ReadOut Device for SiPM. *Physics Procedia*, 37:1569–1576, 2012. doi: 10.1016/j.phpro.2012.02.486.

[32] URL http://omega.in2p3.fr/.

[33] R. Honda et al., editor. *The development of the multi PPD readout electronics with EASIROC and SiTCP*, 2012. Proceedings of Science.

[34] Leo R Dalesio, MR Kraimer, and AJ Kozubal. Epics architecture. In *ICALEPCS*, volume 91, pages 92–15, 1991.

[35] A. Moll. The software framework of the belle II experiment. *J. Phys. Conf. Ser.*, 331 (3):032024, 2011. URL http://stacks.iop.org/1742-6596/331/i=3/a=032024.

[36] S. Agostinelli et al. Geant4—a simulation toolkit. *Nuclear instruments and methods in physics research section A: Accelerators, Spectrometers, Detectors and Associated Equipment*, 506(3):250–303, 2003.

[37] Kohji HIRATA et al. An introduction to sad. *2nd Advanced ICFA Beam Dynamics Workshop on Aperture-Related Limitations of the Performance and Beam Lifetime in Storage Rings= 2nd Advanced ICFA Beam Dynamics Workshop on Aperture-Related Limitations of the Performance and Beam Lifetime in Storage Rings*, pages 62–65, 1998.

[38] R. Kleiss and H. Burkhardt. BBBREM: Monte Carlo simulation of radiative Bhabha scattering in the very forward direction. *Comput. Phys. Commun.*, 81:372–380, 1994. doi: 10.1016/0010-4655(94)90085-X.

[39] S. Jadach, W. Placzek, and B. F. L. Ward. BHWIDE 1.00: O(alpha) YFS exponentiated Monte Carlo for Bhabha scattering at wide angles for LEP-1 / SLC and LEP-2. *Phys. Lett.*, B390:298–308, 1997. doi: 10.1016/S0370-2693(96)01382-2.